JGR Atmospheres

RESEARCH ARTICLE
10.1029/2021JD036098

Key Points:

- A daytime convective initiation (CI) episode, which is a series of CIs clustered in time and space, was caused mainly by the heterogeneity of instability
- Inhomogeneous instability was caused by mesoscale moisture transport from mesoscale pressure disturbances and ageostrophic winds
- The locations of the CI episodes were sensitive to the evolution of mesoscale pressure disturbances by affecting moisture transport

Correspondence to:
Y. Du,
duyu7@mail.sysu.edu.cn

Citation:
Mai, C., & Du, Y. (2022). Mesoscale moisture transport in determining the location of daytime convection initiations clustered in time and space over southern China. *Journal of Geophysical Research: Atmospheres*, *127*, e2021JD036098. https://doi.org/10.1029/2021JD036098

Received 26 OCT 2021
Accepted 11 MAY 2022

Mesoscale Moisture Transport in Determining the Location of Daytime Convection Initiations Clustered in Time and Space Over Southern China

Chuying Mai[1,2,3] and Yu Du[1,2,3]

[1]School of Atmospheric Sciences, Sun Yat-sen University, and Southern Marine Science and Engineering Guangdong Laboratory (Zhuhai), Zhuhai, China, [2]Guangdong Province Key Laboratory for Climate Change and Natural Disaster Studies, Sun Yat-sen University, Zhuhai, China, [3]Key Laboratory of Tropical Atmosphere-Ocean System, Sun Yat-sen University, Ministry of Education, Zhuhai, China

Abstract Convective initiation (CI) episodes are defined as a series of CIs that occur in clusters in time and space, and their prediction remains a challenge due to their complex mechanisms. In the present study, high-resolution convection-permitting simulations and observations were conducted to investigate the source of inhomogeneous instability for a cluster of daytime CIs gathering in a northeast-southwest oriented region in South China where the convergence boundary for lifting was not evident. In the region of the CI episode, low-level water vapor was enhanced significantly, which thus induced the heterogeneity of convective available potential energy. The enhanced moisture and instability in the CI episode region were caused by a mesoscale anticyclonic moisture channel. Mesoscale moisture transport formed under both the inertial oscillation of ageostrophic winds and the mesoscale high-pressure disturbances in the daytime. The revealed mechanism is further confirmed by sensitivity experiments, where mesoscale anticyclonic transport is highly sensitive. Water vapor transport was affected by the evolution of mesoscale pressure disturbances and dominated the location and shape of the CI episode. Stronger mesoscale pressure disturbances resulted in the subsequent mesoscale anticyclonic airflow coming from various high-pressure systems and conveying moisture farther east, and therefore, a CI episode occurred farther east by dozens to hundreds of kilometers. The climatology of the daytime CI episode also showed that the various mesoscale moisture transports confined moisture within the CI episode regions under weak convergence.

1. Introduction

Deep moist convection often occurs in South China with severe weather. Accurate and timely prediction of deep moist convection initiation (CI) is important in providing an earlier warning than that provided by rapidly developing thunderstorms, which may help save lives and property. Therefore, CIs in South China have received increasing scientific attention in recent decades (e.g., Du & Chen, 2019a; Wang et al., 2014; Wu & Luo, 2016). However, given the widely varying possible forcing and complex underlying surface effects in South China, simulating or predicting when and where the individual CI is precisely triggered remains a challenge.

Many previous efforts have been made to clarify the mechanisms of CI. Dynamic lifting in the boundary layer driven by synoptic weather systems is a strong favorable forcing for CI, such as shear lines/trough lines (e.g., Weckwerth & Parsons, 2006), synoptic cold and warm fronts (e.g., Wilson & Roberts, 2006) and LLJs (e.g., Du & Chen, 2019a; Du, Chen, Han, Mai, et al., 2020; Moore et al., 2003; Trier et al., 2020). With weak synoptic lifting, mesoscale convergence boundaries (such as gust fronts, horizontal convective rolls, land–sea breezes, drylines, and topographically forced boundaries) may dynamically induce surface-based ascent and are widely found to be precursors to CI in many observational experiments and numerical studies (e.g., Abulikemu et al., 2019; Bai et al., 2019; Birch et al., 2015; Du, Chen, Han, Bai, & Li, 2020; Torri et al., 2015; Weckwerth et al., 2014). Furthermore, the interactions among several mesoscale boundaries provide more favorable conditions with enhanced updrafts for CIs, especially at the “triple point” (e.g., Bai et al., 2019; Trier et al., 2017). Some studies have found that in the absence of identified surface boundaries, air parcels originating above the boundary layer can be uplifted to the level of free convection (LFC) by gravity waves and bores in stable environments (e.g., Parsons et al., 2019; Wilson et al., 2018; Zhang et al., 2020). The CI in such situations is named elevated CI and is found to be associated with elevated moist absolute unstable layers, where convection inhibition (CIN) is reduced (e.g., M. R. Zhang et al., 2019; Trier et al., 2017). In addition, CI under weak dynamic forcing is also observed in thermally unstable preconditions with moderate CAPE and low CIN (e.g., Adler et al., 2011; Balaji & Clark, 1988).

Distinct from the initiation of an individual convective cell, two or more pristine convection initiations clustered in time and space are named convective initiation episodes (CI episodes) and are suggested to have a common mechanism by Wilson and Roberts (2006). CI episodes with widths of hundreds of kilometers and lifetimes of hours are able to develop into highly organized convection systems. Wilson and Roberts (2006) demonstrated that CI episodes during the IHOP (International H_2O Project) were almost distributed near the surface-based or elevated convergence, which were mostly forced by synoptic or gust fronts and synoptic or mesoscale convergence/confluence coupling with abundant instability at middle levels. Previous studies have found that nocturnal CI episodes are usually accompanied by stable stratification and located along strong convergence boundaries near the surface or at elevated levels (e.g., M. R. Zhang et al., 2019; Reif & Bluestein, 2018; Wilson et al., 2018). As a comparison, daytime CIs are contributed by the diurnal cycle of solar heating, which creates favorable thermodynamic conditions and produces an afternoon peak of the occurrence of CI episodes (Lima & Wilson, 2008; Wilson & Roberts, 2006). However, it has seldom been revealed why daytime CIs are concentrated in a certain region. It can be inferred that CI episodes prefer areas with more favorable thermodynamic conditions (Adler et al., 2011), but the source of the extra thermodynamic energy in a certain region remains unclear. Bai et al. (2020a) revealed that daytime CIs prevailed in South China, as did daytime CI episodes. Understanding the mechanisms of the extra instability confined in a certain range over land and advancing our knowledge of where daytime CI episodes might occur are important for precipitation forecasting in South China.

Thermodynamic conditions largely depend on the distribution of temperature and moisture. The evolution of moisture is found to play a key role in CIs (e.g., Bodine et al., 2010; Fabry, 2004, 2006; Weckwerth, 2000). Numerical and observational studies have found that variations in moisture as low as 1 g/kg could make a difference between CI and no CI (Crook, 1996; Weckwerth et al., 1996). GPS-integrated moisture fields could provide useful information for forecasting CI locations, as moisture changes over the previous 3 hr are important at the locations of CIs (Radhakrishna et al., 2015). Moisture transport by LLJs causes absolute unstable layers that promote CI, which are important features for nighttime CIs on the Great Plains and are commonly without boundaries (e.g., Gebauer et al., 2018; Weckwerth et al., 2019). Such a process was also found in eastern China by M. R. Zhang et al. (2019). In South China, CIs become active after the onset of warm-moist monsoon flows and expand northward as the monsoon advances (Bai et al., 2020a). Du and Chen (2019a) and Du, Chen, Han, Mai, et al. (2020) revealed that nocturnal CIs are closely linked to the interaction of LLJs over the South China Sea with coastal terrain, which moistens the low-level boundary layer. Although moisture transport by nocturnal LLJs is usually found to play an essential role in nocturnal CIs, its specific role in daytime CI episodes over South China has been little studied.

The location and timing of CI forecasting is dependent on the preconvective environment associated with moisture transport (Degelia et al., 2018). Adding random perturbations, the representation of moisture transport by LLJs, which create absolute unstable layers, determines the existence of CIs and their locations in WRF models (M. R. Zhang et al., 2019). The sensitivity of uncertainties in the initial state in eastern China found that a larger amount of low-level moisture carried by monsoon southwesterly airflows contributed to earlier CI during the Meiyu season (Luo & Chen, 2015). However, the sensitivity of daytime CIs in South China to moisture transport still needs to be further studied.

On 6 September 2018, several pristine daytime CIs were found to be clustered in time and space over inland South China. This CI episode was found without obvious boundaries and was located in a region with higher convective available potential energy. This heterogeneity of instability was likely mainly caused by the inhomogeneous moisture. Moisture transport was usually found through large-scale airflows such as monsoon flows or LLJs for nocturnal CIs in previous studies (e.g., Bai et al., 2020a; Du & Chen, 2019a; Du, Chen, Han, Mai, et al., 2020; M. R. Zhang et al., 2019), but LLJs were often relatively weak during the daytime and were absent in the present case. Thus, inhomogeneous moisture near the daytime CI episode region may form under other local factors. Regarding the mechanisms of this daytime CI episode, the objectives of this study are as follows:

1. to explore the source of the heterogeneity of moisture or instability;
2. to examine the sensitivity of the revealed source in numerical models as well as the forecasting of daytime CI episodes.

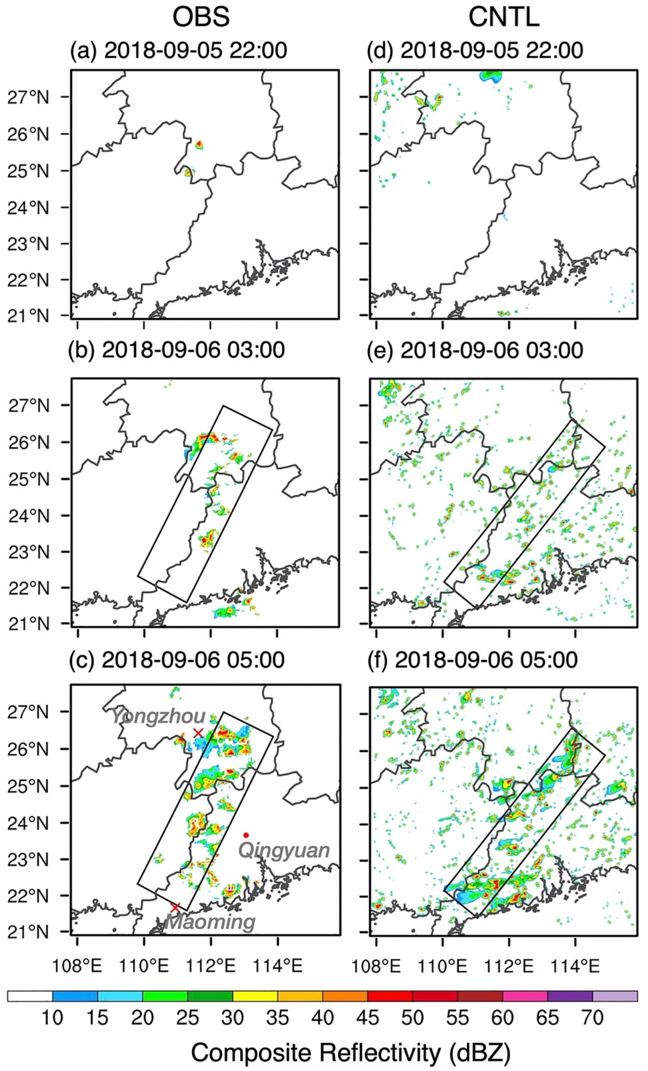

Figure 1. Evolution of composite radar reflectivity (shaded) from (a–c) observation (OBS) and (d–f) WRF simulation (CNTL) at (a and d) 22 UTC 5 September (b and e) 03 UTC 6 September and (c and f) 05 UTC 6 September 2018. Black boxes represent the CI episode regions where convections were initiated in clusters. The red dot in (c) indicates the location of the sounding profile at Qingyuan, and the red crosses indicate the locations of cities mentioned in the paper.

The rest of this paper is organized as follows. A general case overview of this CI episode is given in Section 2. Section 3 briefly introduces the model configurations and evaluations. In Section 4, the thermodynamic heterogeneity of CI episodes is investigated. Section 5 and Section 6 examine the source of inhomogeneous moisture and the formation of the associated mesoscale transport, respectively. Section 7 examines the sensitivity of the source revealed above to initial conditions and explores its influence on CI episodes. Section 8 presents the climatology of the daytime CI episode to discuss the universality of the event and the revealed mechanisms. Finally, the main results are summarized and discussed in Section 9.

2. Case Overview

At 03 UTC (11 LST = UTC + 08) on 6 September 2018, various convection cells were triggered close in time and were confined along a line-shaped region where no nearby convection had occurred before (Figures 1a and 1b). CI is defined as radar reflectivity first reaching 40 dBZ over an area of at least 8 km^2, which has been widely used as a criterion in previous studies (e.g., Bai et al., 2020b; Lima & Wilson, 2008; Wang et al., 2014; Wilson & Roberts, 2006). Mosaic radar products with a 6-min temporal resolution obtained from CINRAD radars are used in the present study to identify CI. Wilson and Roberts (2006) called such a series of CIs clustered in time and space a CI episode. A linear CI episode was observed in western Guangdong (Figure 1c) in an orientation of SW-NE and a size of approximately 550 × 200 km from Maoming City to Yongzhou City (indicated by crosses).

Figures 2a–2d shows the synoptic circulations at 00 UTC 6 September, 3 hr ahead of the linear CI episode, using the 0.25°-spacing National Centers for Environmental Prediction Final Analysis (NCEP FNL) Operational Global Analysis data. Northeasterly flows prevailed in the CI episode area, which was located southeast of the South Asia high at 200 hPa (Figure 2a). Located in the southwestern region of the western Pacific subtropical high (WPSH, indicated by "H"), the studied linear episode area was dominated by easterly winds at 500 hPa and southeasterly winds at 700 hPa (Figures 2b and 2c). The WPSH induced downward motions and dynamically inhibited convections. At 850 hPa, southeasterlies near the CI episode area were caused by flows northeast of a low-pressure disturbance (indicated by "L") in the South China Sea (Figure 2d), which contributed to the transport of water vapor from the sea to Guangdong. A weak shear line (indicated by the red line in Figure 2d) formed at the terminus of the southeasterlies near the CI episode, but the associated convergence was weak (shown in Section 4). Meanwhile, the southwest vortex (indicated by "SWV") was located in the west, and the subtropical high was located in the east. These pressure and flow patterns at 925 hPa were similar to those at 850 hPa (not shown). Before the CI episode, no obvious strong synoptic convergence system was found near the CI episode region.

Figure 3a shows a radiosonde sounding released at Qingyuan station (red dot in Figure 1c) at 00 UTC 6 September, illustrating the vertical thermodynamic preconvective environment near the CI episode region. A temperature inversion layer occurred near the surface due to radiative cooling at night, while a deep moist layer existed below 600 hPa. In addition, a nearly saturated inversion layer occurred at approximately 800 hPa. This stratification provided a thermodynamically favorable condition for CI with a moderate surface-based CAPE of 1,399.02 J kg^{-1}, low surface-based CIN of 15.66 J kg^{-1} and low LFC at 849.60 hPa.

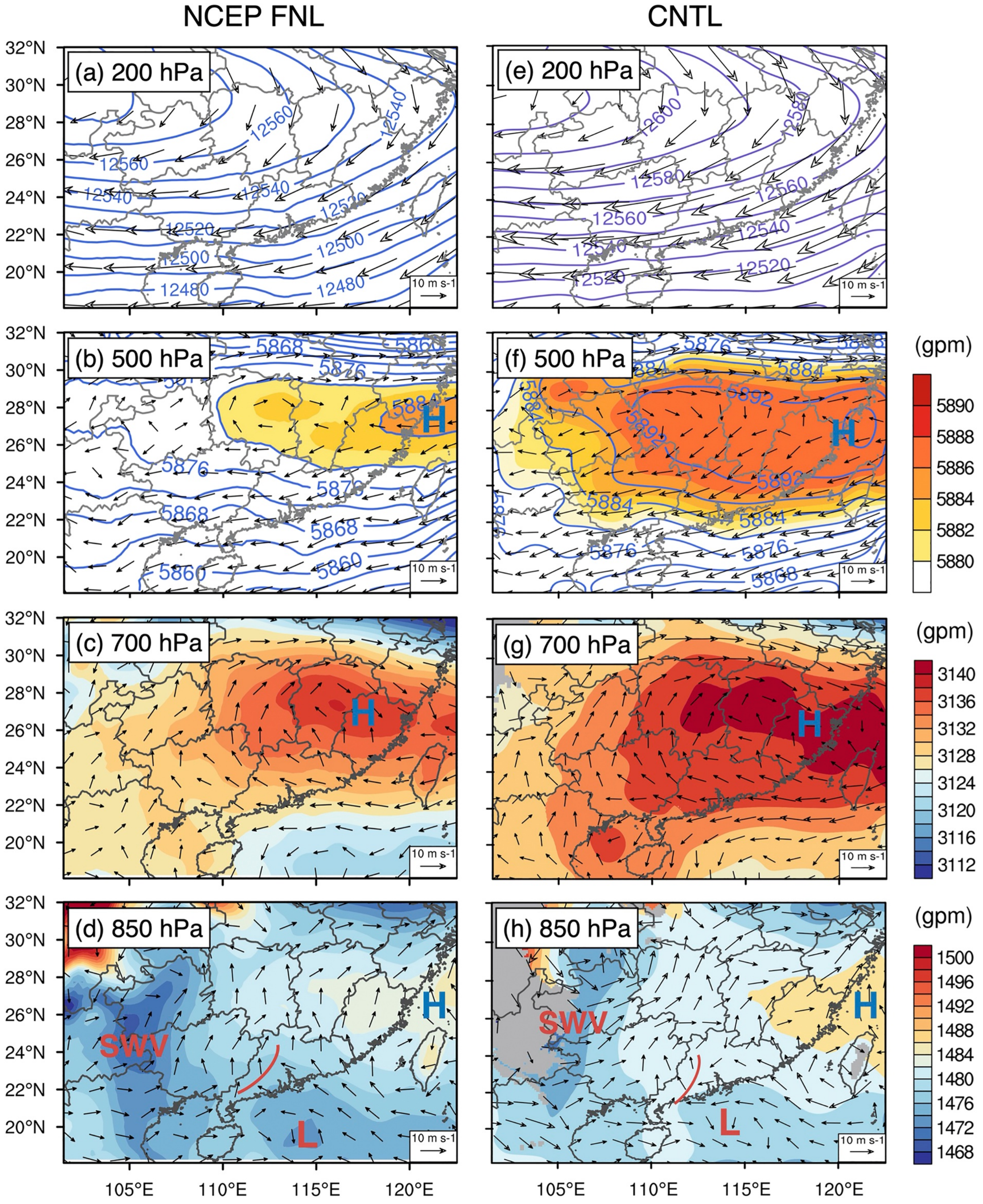

Figure 2. Horizontal distribution of geopotential height (contour and shaded) and horizontal wind fields (vector) from (a–d) NCEP FNL reanalysis data (NCEP FNL) and (e–h) WRF simulation (CNTL) (a and e) at 200 hPa (b and f) at 500 hPa (values higher than 5,880 m are shaded) (c and g) at 700 hPa and (d and h) at 850 hPa at 00 UTC on 6 September 2018. The red line indicates a shear line at 850 hPa. “SWV”, “L” and “H” indicate the locations of the southwest vortex, low-pressure disturbance and subtropical high, respectively.

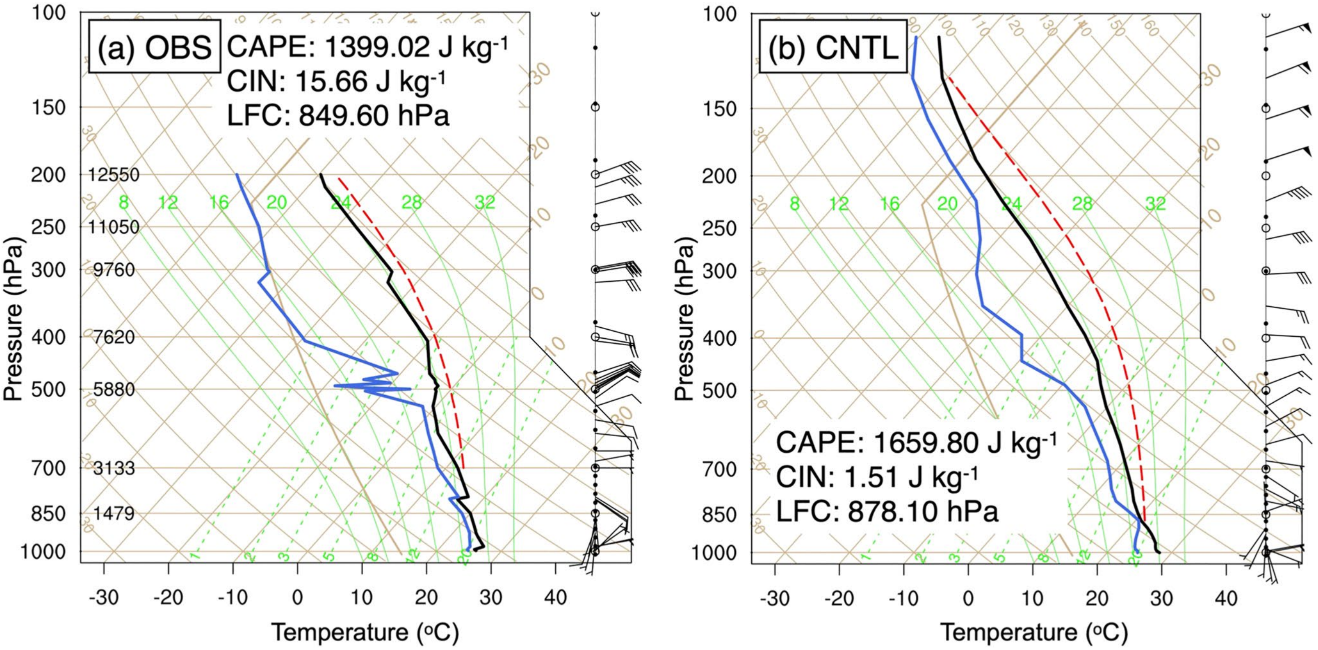

Figure 3. Skew T-logp diagrams of sounding released at Qingyuan station (red dot shown in Figure 1c) in (a) observation (OBS) and (b) WRF simulation (CNTL) at 00 UTC 6 September 2018. The solid black and blue line indicate the ambient temperature and dewpoint temperature profiles, respectively. The CAPE, CIN and LFC of parcels lifted from the surface are shown in the diagrams.

A series of daytime CIs occurred close in time and confined in a line-shaped area with no favorable synoptic forcing but with fairly thermodynamic conditions. To clearly elucidate the differences between the CI episode region and the other regions, high-resolution WRF simulations were performed and are analyzed below.

3. Configurations and Evaluations of the WRF Simulation

3.1. WRF Model Configurations

To understand the mesoscale physical processes under the CI episode in detail, a high-resolution (4 km) simulation was conducted with WRF model version 4.0. The simulation used a one-way nested grid configuration for two domains with horizontal spacings of 12 km (d01) and 4 km (d02) (Figure 4). Both domains had 33 vertical layers in the terrain-following η coordinate. The MYJ PBL scheme was found to produce smaller mean errors of MLCAPE and MLCIN forecasts and gave more realistic results than the YSU scheme (Coniglio et al., 2013; Otkin & Greenwald, 2008). Moreover, referring to some numerical studies on CIs near South China that generally reproduce convection processes well (e.g., Du, Chen, Han, Mai, et al., 2020; Zhang et al., 2021), the simulation used the following physical parameterization schemes. The two domains were configured by the Thompson microphysics scheme (Thompson et al., 2008), Mellor–Yamada–Janjic (MYJ) boundary layer scheme (Janjić, 1994), longwave rapid radiative transfer model for the GCM (RRTMG) radiation scheme, shortwave RRTMG radiation scheme (Iacono et al., 2008) and Noah land surface model (Ek et al., 2003), while the Kain-Fritsch cumulus scheme (Kain, 2004) was only applied in the outer domain. Combinations with other parameterization schemes were also used, and the chosen parameterization schemes showed a better representation of the CI episode. The NCEP FNL data were used as the initial and boundary conditions to drive the model. The simulation was initialized at 12 UTC 5 September 2018, which was 9 hr prior to the occurrence of the CI episode that allowed the model to spin up.

3.2. Evaluation of the WRF Simulation

Figure 1 compares the performance of the high-resolution WRF simulation (hereafter CNTL) to observations with regards to the series of CIs clustered linearly in South China. As detected by radar, almost no convection occurred over South China at 22 UTC 5 September in the simulation, and several hours later, scattered convection

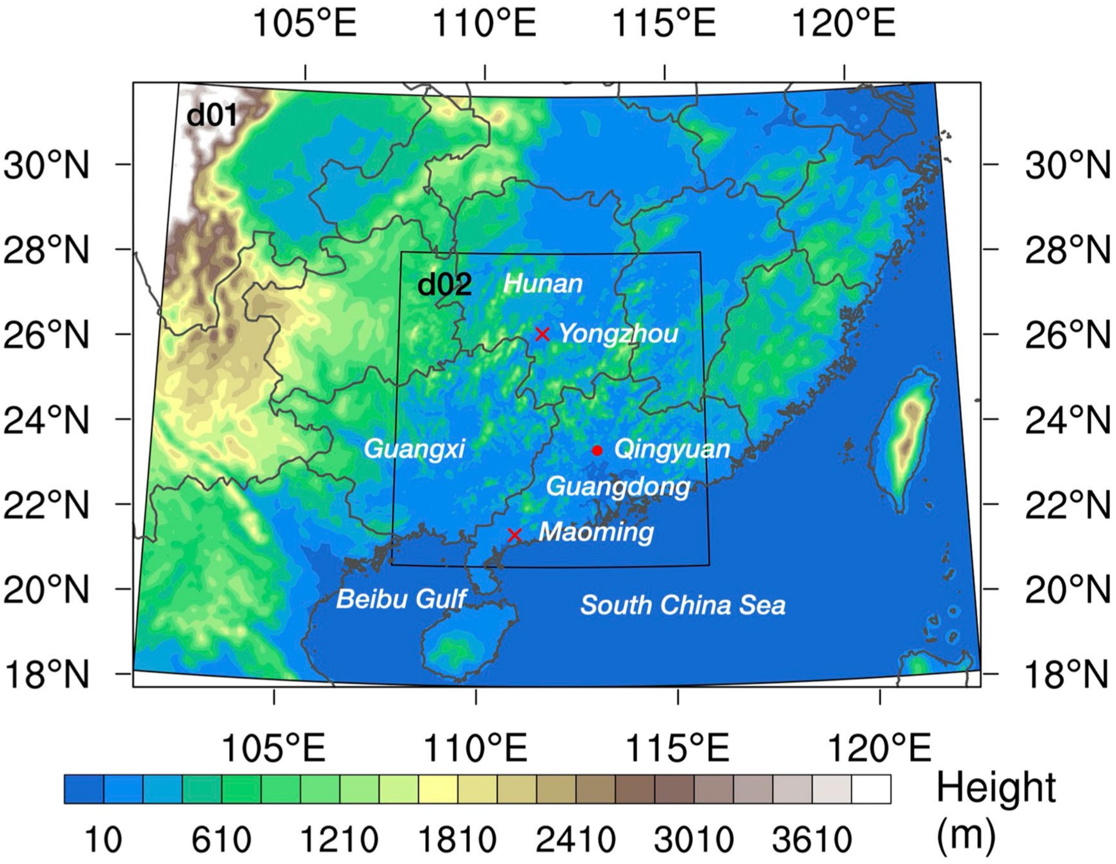

Figure 4. Simulated domains (d01 and d02) and terrain height (shaded) in South China. The red dot indicates the location of the sounding profile at Qingyuan. The red crosses indicate the locations of cities mentioned in the paper.

cells were simulated (Figures 1d and 1e). Too many small and weak scattered CIs occurred over all of South China in the simulation, but they were not observed in the radar observations due to the inability of the radar to detect weak convections that were located away from radars and were lower than the lowest elevation or due to the bias producing too many small convections in the models (e.g., Burghardt et al., 2014; Henderson et al., 2021). The model overproduction of CI might be caused by the common use of the physical parameterizations that are not ideally suited for use with horizontal grid spacings capable of explicitly resolving deep moist convection, which possibly leads to CI errors by impacting the thermodynamic conditions prior to and during CIs (Burghardt et al., 2014). However, dense and larger CIs occupying more than 8 km^2 were clustered in a linear-shaped area (CI episode region, Figure 1e), which was similar to the observation. Simulated CIs in the northern portion of the CI episode region were shifted eastward (~140 km) with errors in Hunan Province. A small bias in the orientation (~9°) of the CI episode region was thus involved in the simulation, which made the region more zonally oriented. Overall, the simulated CI episode was generally reproduced with a similar shape and at a similar position at the same time (cf. Figures 1c and 1f).

The simulated synoptic background patterns were generally consistent with the reanalysis. Similarly, the South Asia high at 200 hPa was located to the northwest of the CI episode region in the CNTL (Figure 2e). The WPSH at 700-500 hPa dominated South China in the simulation but with a larger strength (Figures 2f and 2g). At a lower level, cyclonic flows existed over the South China Sea as well but with a weaker intensity, and the weak shear line was also reproduced near the CI episode region (Figure 2h). A generally similar vertical stratification at Qingyuan was reproduced by the simulation as the observed soundings, where a similar nearly moist layer occurred at 850 hPa, although the temperature inversion layer near the surface was missed by the model. The simulated surface CAPE (1,659.80 J kg^{-1}), CIN (1.51 J kg^{-1}) and LFC (1,201 m or 878.10 hPa) at Qingyuan showed moderate CAPE, low CIN and low LFC similar to the observations (Figure 3b).

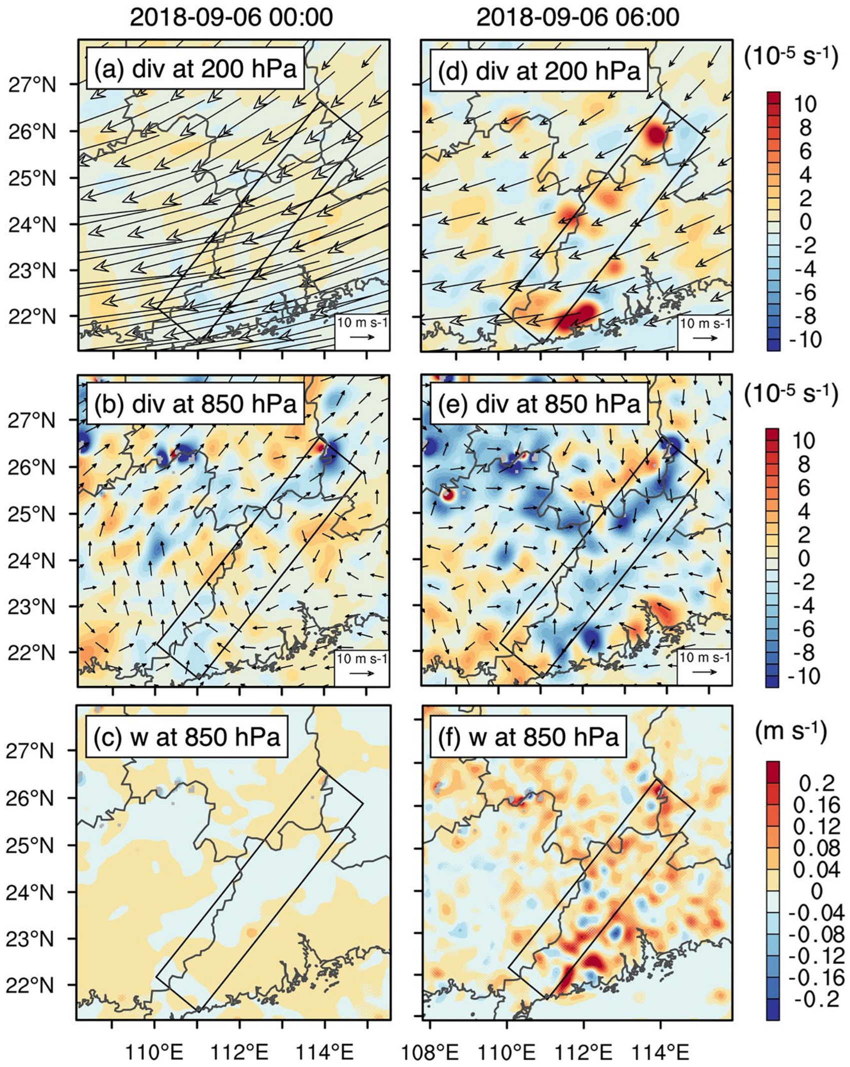

Figure 5. Evolution of WRF-simulated divergence (shaded, units: 10^{-5} s^{-1}) and horizontal wind fields (vector) (a and d) at 200 hPa (b and e) at 850 hPa, and (c and f) vertical velocity (w, shaded, units: m s^{-1}) at 850 hPa at (a–c) 00 and (d–f) 06 UTC 6 September 2018. Black boxes represent the CI episode region.

According to the evaluations above, the simulation captured the occurrence and shape of the CI episode accompanied by the weak synoptic preconvective environment and unstable thermodynamic structure well. Therefore, it is reasonable to explore the differences in the CI episode region and the other regions using this high-resolution simulation.

4. Thermodynamic Heterogeneity in the CI Episode

Since the CI episode had a relatively wide range and commonly occurred under the same mechanism, the present section compares the differences between the CI episode region and neighboring regions to clarify the physical processes controlling where a cluster of CIs would be confined.

Although many previous studies have demonstrated that CI episodes are approximately distributed along the surface-based or elevated lifting (e.g., M. R.; Zhang et al., 2019; Reif & Bluestein, 2018; Wilson et al., 2018; Wilson & Roberts, 2006), Figure 5 presents the absence of near-surface or elevated convergence boundaries near the CI episode region. Before the CI episode (00 UTC 6 September), both the divergence at 200 hPa (Figure 5a) and convergence at 850 hPa (Figure 5b) were relatively weak in the line-shaped CI episode region (black boxes). Despite the existence of a shear line near the CI episode (Figure 2h), convergence at low levels ($<5 \times 10^{-5}$ s^{-1})

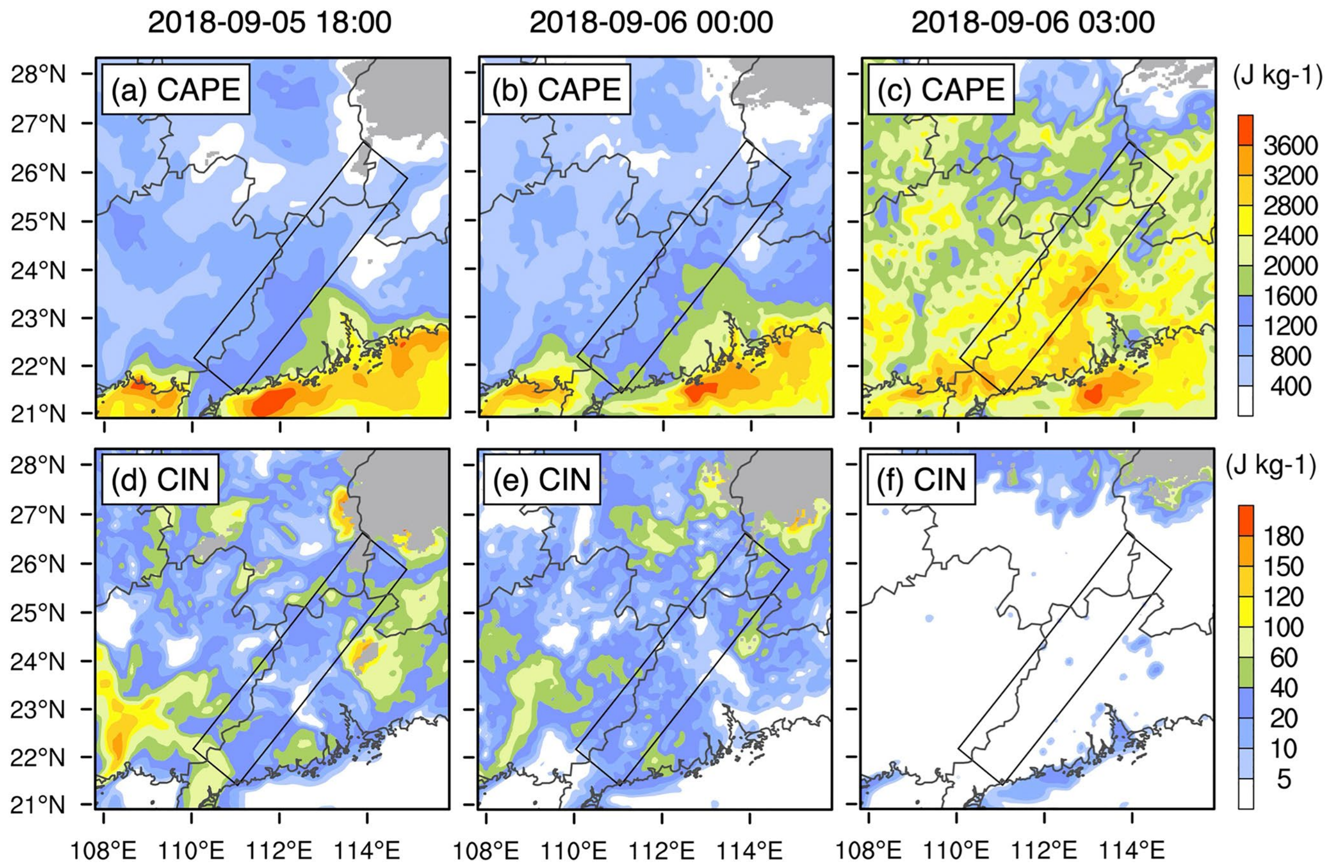

Figure 6. Evolution of WRF-simulated (a–c) CAPE and (d–f) CIN at (a and d) 18 UTC 5 September (b and e) 00 UTC 6 September, and (c and f) 03 UTC 6 September 2018. Black boxes represent the CI episode region.

was weaker than the unfavorable convergence condition ($1 \times 10^{-4}\ s^{-1}$) for CI found in M. R. Zhang et al. (2019). Divergence at low levels were even stronger than that at high levels in most portions of the area. Differences in preconvective convergence and lifting between the CI episode region and other regions did not exist, whereas strong convergence and updrafts became significant in the CI episode after triggering as a result of positive feedback from convections.

Nevertheless, significant differences in thermodynamics between the CI episode region and the vicinity can be seen in Figure 6. The surface-based CAPE increased after sunrise and reached a higher value in the CI episode region, which provided a more unstable environment than the vicinity at 03 UTC 6 September when the CI episode occurred (Figures 6a–6c). The surface-based CIN gradually decreased to nearly zero throughout South China prior to CI (Figures 6d–6f). Larger CAPE and negligible CIN in the CI episode area indicated that the air parcel could have been lifted up to overcome CIN easily and could then have released stronger CAPE in the CI episode region for denser and larger CIs. Different from the relatively even distribution of negligible CIN over South China, the heterogeneity of CAPE between the CI episode region and the other regions suggests the dominant role of CAPE in the CI episode location in the current case. In contrast, Adler et al. (2011) documented in a case in West Africa that the location of CIs was controlled by inhomogeneous CIN.

To further clarify the reasons for the heterogeneity of instability in the CI episode region, Figure 7 further illustrates the temporal evolution of the vertical profiles of dynamic and thermodynamic variables averaged over the CI episode area (black box in Figures 1e and 8a) and the less-CI area (red box in Figure 8a). In the CI episode region, divergence at low levels accompanied by downward motions was present until the CI episode occurred (Figure 7a), indicating an unfavorable preconvective dynamic environment. At the triggering time (~03 UTC), updrafts were rooted near the surface in the boundary layer, suggesting surface-based CIs. The average CAPE increased significantly 3 hr prior to the CI episode (~00 UTC) and reached 2400 J kg^{-1} near the surface 1 hr

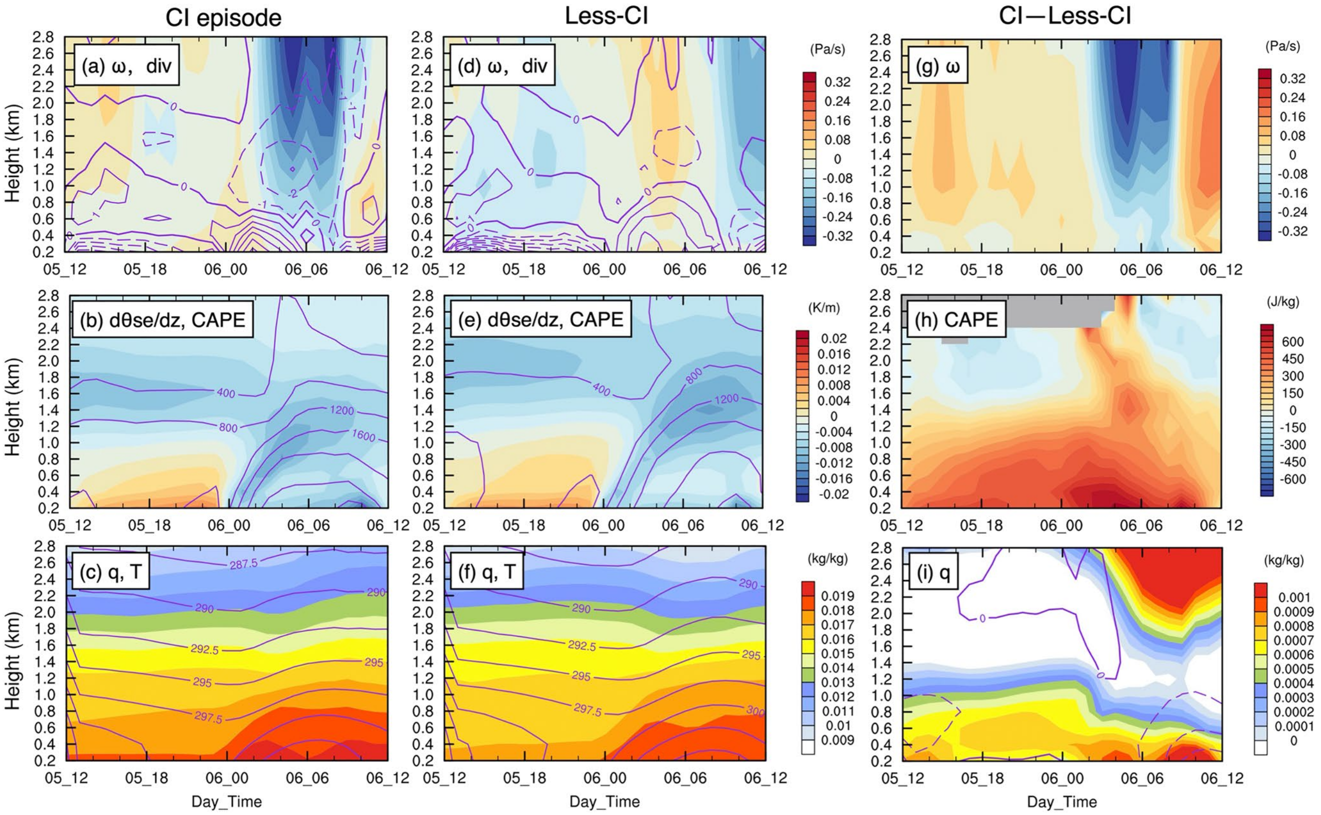

Figure 7. Temporal evolution of the vertical profiles of spatially averaged (a) vertical motion (ω, shaded, units: Pa s^{-1}), divergence (contour, every 1×10^{-5} s^{-1}, units: 10^{-5} s^{-1}), (b) vertical gradient of pseudoequivalent potential temperature (dθ_{se}/dz, shaded, units: K m^{-1}), CAPE (contour, every 400 J kg^{-1}, units: J kg^{-1}), (c) specific humidity (shaded, units: kg kg^{-1}), and temperature (contour, every 2.5 K, units: K) over the CI episode area (shown as a black box in Figure 8a) (d–f) Same as (a–c) except for over the less-CI area (shown as a red box in Figure 8a). Differences in (g) vertical motion, (h) CAPE and (i) special humidity (shaded) and temperature (contour, every 1 K) between the CI episode and less-CI region. Positive values are shown as solid lines, and negative values are shown as dashed lines.

prior to the CI episode (~02 UTC, Figure 7b). Another diagnosed thermal variable is the vertical gradient of the potential pseudoequivalent temperature (θ_{se}), which is calculated based on the Bolton equation (Bolton, 1980):

$$\theta_{se} = t_k \left(\frac{1000}{p}\right)^{0.2854(1.0-0.28q)} \times e^{\left(\frac{3376}{t_{lcl}}-2.54\right)q(1.0+0.81q)}$$

where t_k is the absolute temperature, p is the pressure, q is the specific humidity, e is the base of the natural logarithm, and t_{lcl} is the absolute temperature at the lifting condensation level (LCL). t_{lcl} is obtained from $t_{lcl} = \frac{2840}{3.5 \ln t_k - \ln e - 4.805} + 55$, where e represents the vapor pressure obtained from $e = \frac{pq}{0.622+q}$. The negative vertical gradient of θ_{se} continued to increase after 00 UTC above the surface, which corresponded to the enhanced CAPE. As a comparison, similar variables were examined over the less-CI region (Figures 7d–7f, red box in Figure 8a). In the less-CI region, fewer scattered CIs were observed compared with the CI episode region (Figures 1e and 1f and 8a). The less-CI region was also characterized by an increase in CAPE or a negative vertical gradient of θ_{se} near the surface after 00 UTC due to radiation but with a much lower magnitude (e.g., CAPE of 1600 J kg^{-1} at 02 UTC) than those in the CI episode region (Figures 7b and 7e). The differences between the CI episode region and the less-CI region more clearly show the even stronger downward motions in the preconvective environment of the CI episode region, as well as the more unstable environment featured by larger instability at low levels, which contributed to more clustered CIs there compared with the less-CI region (Figures 7g and 7h).

The distributions of CAPE largely depend on the vertical structure of temperature and moisture in the CBL (e.g., Adler et al., 2011; Crook, 1996). To clarify the dominant factors contributing to the extra unstable environment in the CI episode region, the diurnal variations in temperature and specific humidity in the vertical cross section were examined (Figures 7c, 7f and 7i). The surface and near-surface atmospheres in the two

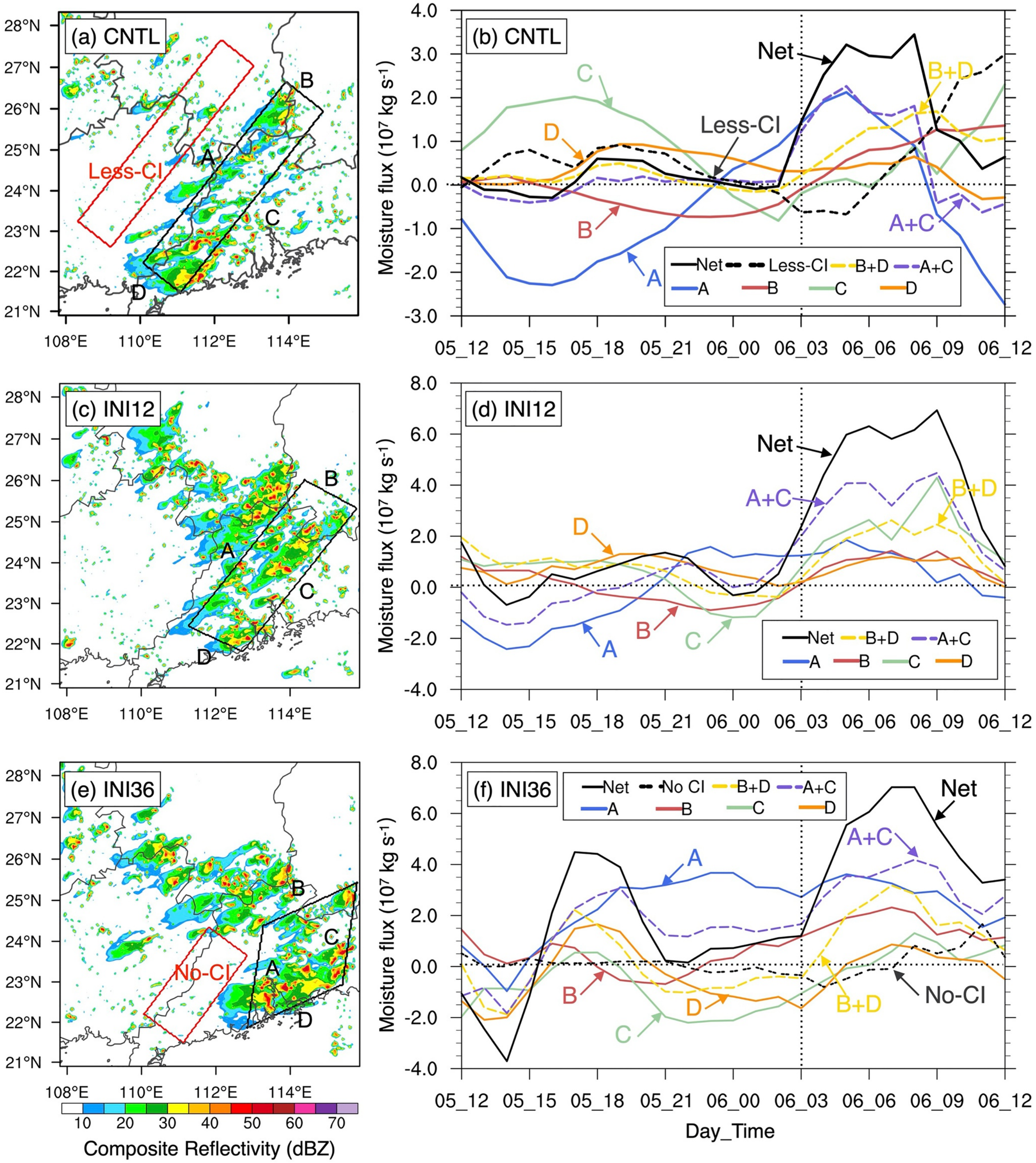

Figure 8. (a) Simulated composite reflectivity at 07 UTC 6 September and (b) temporal evolution of net moisture fluxes into the regions (shown as boxes in a) and moisture fluxes through four boundaries of the CI episode region in the CNTL (c and d) Same as (a and b) except for INI12 at 06 UTC 6 September (e and f) Same as (a and b) except for INI36 at 06 UTC 6 September. Black boxes represent the CI episode regions, while red boxes mark the less-CI regions.

regions were heated to a close temperature due to solar radiation (Figure 7c). An even higher near-surface temperature was observed in the less-CI region after 05 UTC (Figure 7i). Meanwhile, the low level in the CI episode region was moistened to an average of 0.019 kg/kg after 00 UTC, and the moist layer was deepened (Figure 7c). However, the enhancement of moisture was less obvious in the lower CI region (Figure 7f). More moisture was transported into the CI episode region, which resulted in larger instability accumulation than in the less-CI region, further resulting in multiple CIs clustered in the linear region in the weak lifting environment (Figures 7h and 7i).

Therefore, the current case displayed the inhomogeneous moisture distribution between the CI episode region and the surrounding regions, which resulted in the corresponding heterogeneity of instability and thus the clustered CIs within the linear CI episode region. We will further discuss the source of the inhomogeneous moisture through moisture budget analysis in the following sections.

5. Source of the Inhomogeneous Moisture

To investigate the source of the additional enhancement in low-level moisture, the moisture budget in the CI episode region (black box in Figure 8a) was analyzed. Moisture fluxes were calculated based on the equation shown by Y. Zhang et al. (2019) and Du and Chen (2019b):

$$Q = \int_{z_s}^{z_t} \int_{x_1}^{x_2} (\rho q_v V_n)\, dx\, dz$$

where ρ, q_v, and V_n are the air density, specific humidity, and velocity at every boundary, respectively. A positive value of moisture flux indicates the direction into the region. Since most water vapor was concentrated below 2.0 km (>0.013 kg kg^{-1}, shown in Figure 7c), the moisture fluxes were integrated from the surface z_s to $z_t = 2$ km and from the beginning x_1 to the end x_2 of the boundary.

As shown in Figure 8b, the net moisture flux in the CI episode region or less-CI episode region was nearly zero from 12 UTC 5 September to 00 UTC 6 September. After 02 UTC 6 September, the net moisture flux was negative in the less-CI region near the CI timing, and moisture did not accumulate. In the CI episode region, the net moisture flux started to increase significantly and reached a comparatively high value of nearly 3.2×10^7 kg s^{-1} near 05 UTC 6 September. The sum of the moisture fluxes through boundaries A and C played a dominant role in net moisture fluxes in the CI episode region after 02 UTC 6 September. Before 23 UTC 5 September, the moisture fluxes through boundary A (negative) and boundary C (positive) were nearly symmetric, and their contributions canceled out each other in regard to the net fluxes because strong southeasterlies carried moisture from the South China Sea into the CI episode region through boundary C and out from boundary A. After 23 UTC 5 September, the directions of moisture fluxes through boundaries A and C were reversed due to winds changing from southeasterlies to northwesterlies, which suggests that moisture flowed into (out of) the region through boundary A (C). After 02 UTC 6 September, more moisture was transported into the region through boundary A from the Beibu Gulf, but less moisture flowed out of the region through boundary C. The northwesterly moisture transport was blocked and resulted in net moisture stored in the CI episode region.

The horizontal distributions and evolution of moisture fluxes at 925 hPa are further presented in Figures 9a–9c. Before 21 UTC 5 September, southeasterly winds carried water vapor from the South China Sea into (out of) the region through boundary C (boundaries A and B) (Figures 9a and 9b). On the western side, the southwesterlies nearly parallel to boundary A could not bring water vapor into the CI episode region, resulting in nearly zero net moisture fluxes into the region (Figure 8b). After 21 UTC on 5 September, the southwesterly wind near boundary A gradually veered to westerlies or northwesterlies and formed a mesoscale anticyclonic circulation (indicated by the thick blue vector in Figures 9b and 9c). The northwesterly flow was perpendicular to boundary A and water vapor was from the Beibu Gulf into the CI episode region (Figure 9c). Moisture was transported into the CI episode region through mesoscale anticyclonic transport and then flowed in a northeastward direction parallel to boundary C, which resulted in positive net moisture flux in the CI episode region (Figure 8b).

The above analysis of moisture fluxes in the simulation reveals that the veering mesoscale anticyclonic airflow transported moisture into the episode region, where convection was densely triggered. These processes can be further validated by surface in situ station observations, despite smaller-scale disturbances near the surface (Figure 10). The observed surface wind was averaged over 10 min and available every 5 min. Near and parallel to the western border of the episode region (dashed-line box), the southwesterly surface winds gradually rotated to westerlies or northwesterlies before 02 UTC and formed a mesoscale anticyclonic circulation (indicated by

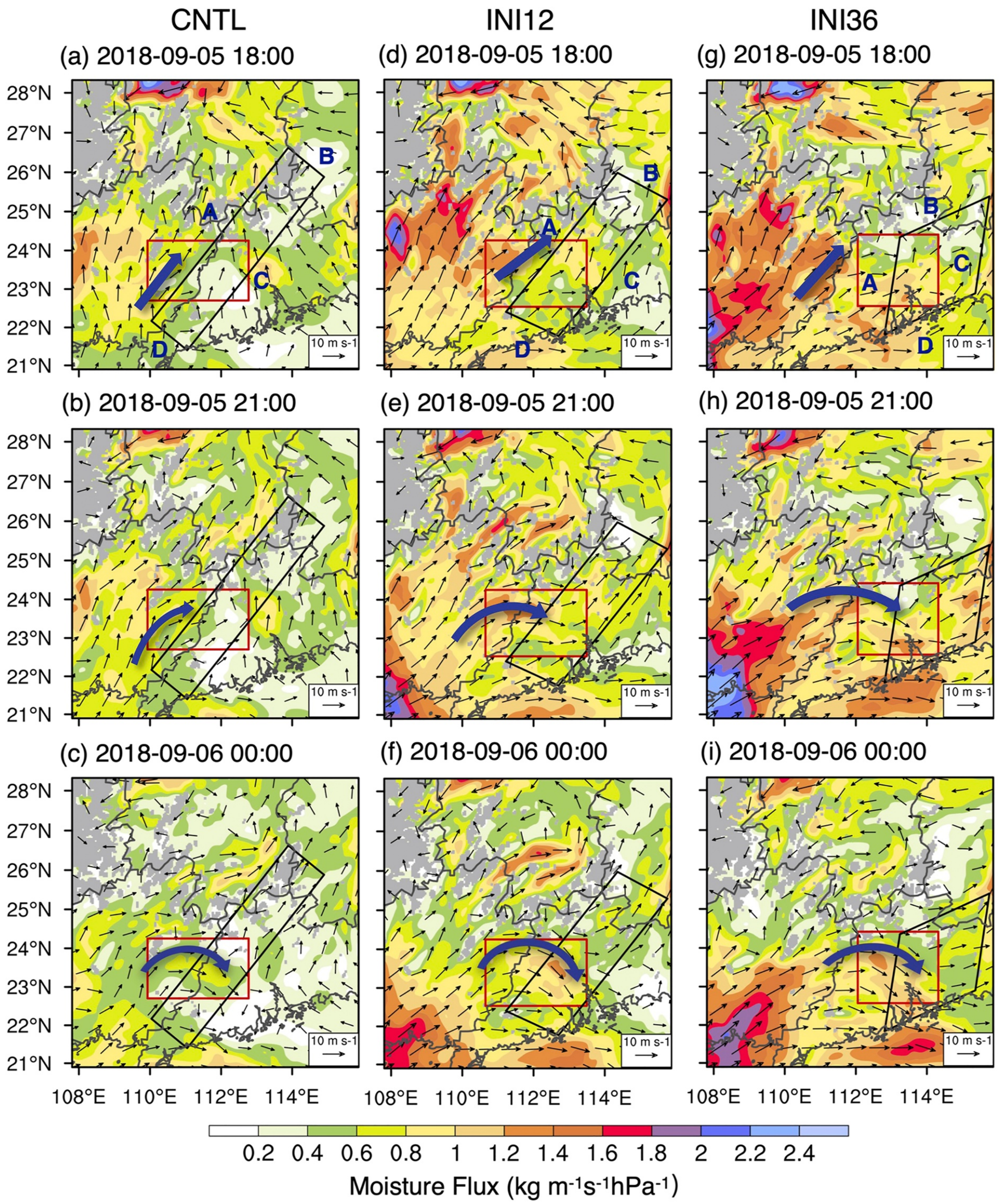

Figure 9. Evolution of simulated moisture fluxes (shaded) and horizontal wind fields (vector) at 925 hPa (a, d, g) at 18 UTC and (b, e, h) 21 UTC 5 September and (c, f, i) 00 UTC 6 September in the (a–c) CNTL (d–f) INI12, and (g–i) INI36 runs. Black boxes represent the CI episode regions, and red boxes represent the locations of mesoscale anticyclonic airflow in each experiment. Thick blue vectors represent veering anticyclonic airflow.

blue vectors in Figures 10c–10e). Then, it converged with the winds near the eastern border. Figure 11a presents the evolution of surface winds averaged in the region of diversion, where the background southwesterlies veered obviously clockwise and a mesoscale anticyclonic flow formed. It clearly shows that surface winds rotated clockwise from southeasterlies to southwesterlies, which resulted in enhancement of the component into the western

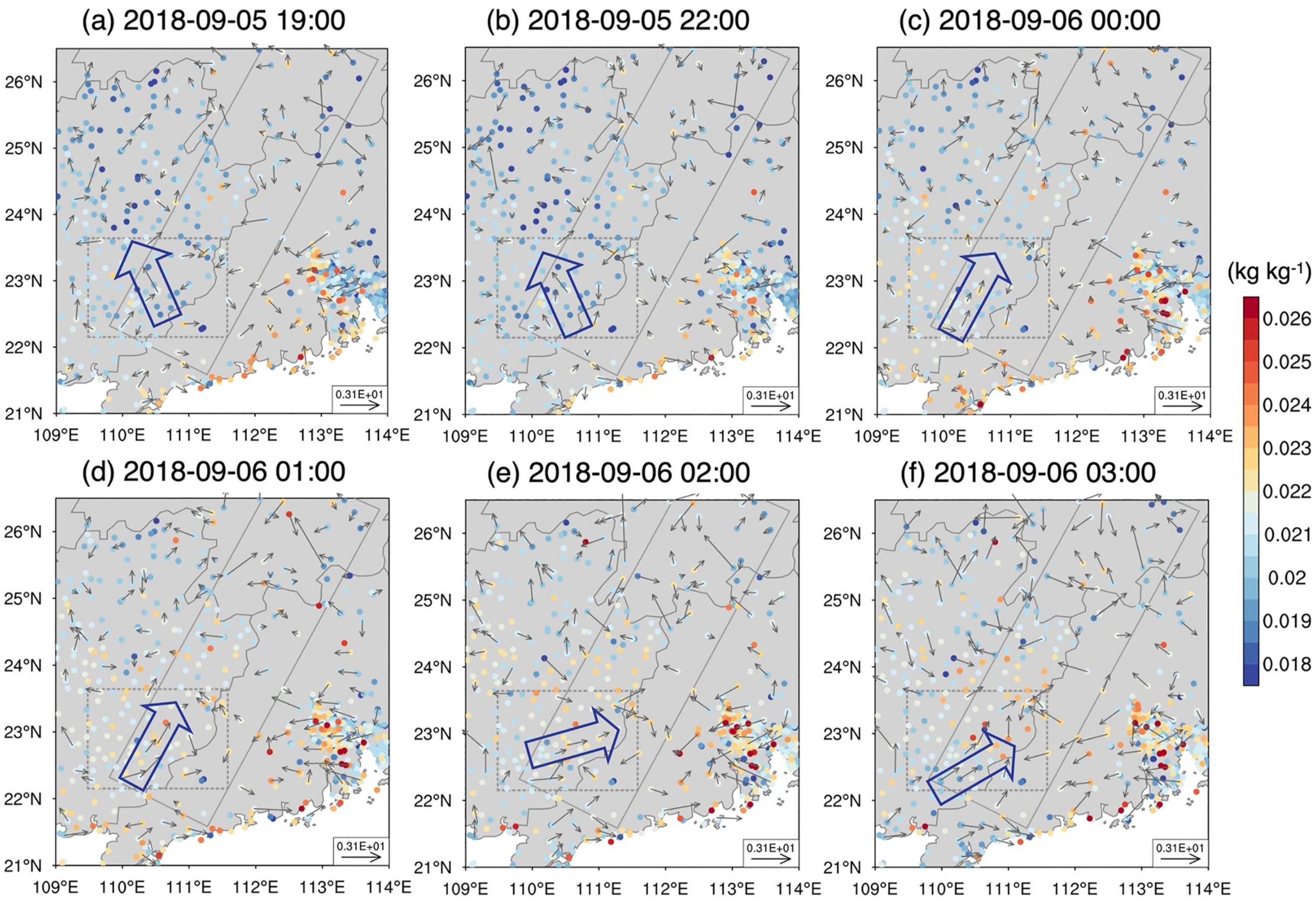

Figure 10. Evolution of observational 10-min average surface wind (vector) and specific humidity (dot) derived from surface in situ weather stations over South China at (a) 19 UTC and (b) 22 UTC 5 September and (c) 00 UTC, (d) 01 UTC, (e) 02 UTC and (f) 03 UTC September 6. Boxes with solid lines in (a–f) represent the location of the observed CI episode region, and dashed lines represent the location of mesoscale anticyclonic airflow. The thick blue vectors represent the veering airflows.

boundary (Figure 11a). Accompanied by the diversion of winds, the specific humidity increased significantly in the observed CI episode region, which created a more favorable thermodynamic environment for CIs gathering (Figures 10d–10f).

6. Formation of Mesoscale Moisture Transport

The evolution of low-level mesoscale circulations is shown in Figure 12 to be associated with the formation processes of mesoscale anticyclonic moisture transport. A low-pressure vortex (indicated by "L") occurred over South China, and subtropical high pressure (indicated by "H") surrounded it on the eastern side (Figure 12a). After 20 UTC 5 September, as the subtropical high pressure strengthened and extended into South China, the low-pressure vortex was correspondingly weakened and separated out into two weak, smaller-scale, low-pressure disturbances over Hunan Province and the South China Sea (Figures 12b and 12c). Then, the subtropical high pressure retreated back to the east. Meanwhile, the low-pressure vortex strengthened and the two divided low-pressure disturbances merged into a low-pressure center (Figure 12d). The merged low-pressure center in Guangdong Province separated out a mesoscale high-pressure center in Guangxi Province from the vicinity of subtropical high pressure (Figure 12d). The mesoscale anticyclonic circulation associated with the mesoscale high-pressure center then transported moisture into the CI episode region (Figures 9c and 12d).

The diversion of southwesterlies and the formation of anticyclonic moisture transport began before the formation of the mesoscale high-pressure center (Figures 9b and 12d), which implies the existence of geostrophic adjustment. To examine the contributions of geostrophic winds and ageostrophic winds to the formation of mesoscale

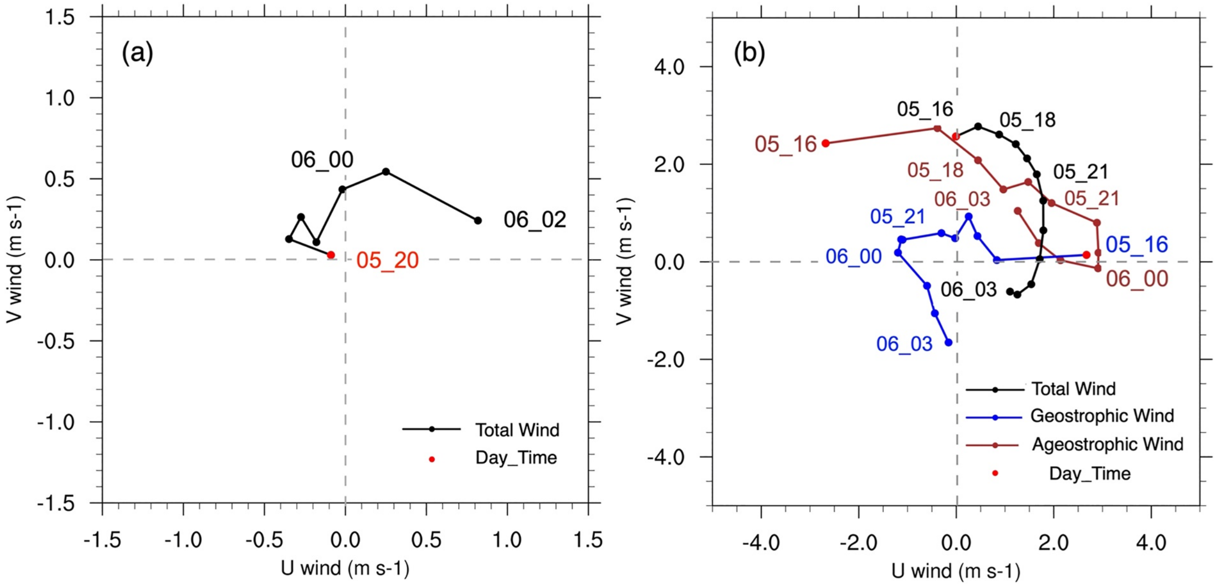

Figure 11. Hodographs of spatially averaged (a) observational 10-min average surface wind over the dashed-line box in Figure 10 and (b) filtered total winds (black curve), geostrophic winds (blue curve) and ageostrophic winds (red curve) at 925 hPa over the red box in Figure 9c in CNTL. The dots represent corresponding hours beginning at (a) 20 UTC and (b) 16 UTC 5 September.

anticyclonic transport, they were further separated with a method used in Xue et al. (2018). The geostrophic winds were calculated from the filtered geopotential height fields, which were filtered with a low-pass Barnes filter (Barnes, 1964) to damp waves shorter than 500 km and retain waves longer than 1,000 km. The ageostrophic winds were left by filtered total winds minus computed geostrophic winds. The hodographs of total, geostrophic and ageostrophic winds averaged in the anticyclonic transport area (red box in Figures 9c and 12e) are presented in Figure 11b. The geostrophic winds were parallel to the geopotential height contours and changed with their evolution (Figure 12e). The total winds associated with mesoscale anticyclonic transport rotated clockwise from 16 UTC 5 September to the time of CI (black curve in Figure 11b). However, geostrophic winds over the anticyclonic area (blue curve) rotated anticlockwise and contributed negatively to the clockwise rotation of total winds, as the high-pressure disturbance was not yet isolated over Guangxi Province before 00 UTC 6 September. According to inertial oscillation theory in the boundary layer (Blackadar, 1957; Xue et al., 2018), the winds were enhanced at night, and the ageostrophic winds evidently rotated clockwise with time, which resulted in winds turning from southwesterlies to westerlies (before 00 UTC) and thus transporting moisture eastward into the CI episode region during nighttime. With the formation of isolated high-pressure disturbance during daytime (after 00 UTC), geostrophic winds were adjusted from easterlies to northeasterlies over the anticyclonic circulation area (Figures 12d and 11b). Total winds were influenced by the strong southward component of geostrophic winds and shifted to northwesterlies, conveying moisture from the Beibu Gulf into the CI episode region. The formed mesoscale anticyclonic transport brought extra enhancement of humidity and instability in the CI episode region, where the series of CIs clustered in time and space.

7. Sensitivity of Mesoscale Moisture Transport

As shown in Section 6, the evolution of mesoscale pressure disturbances generated mesoscale anticyclonic moisture transport, which caused the heterogeneity of moisture and instability accumulation between the CI episode region and other regions. To examine the sensitivity of this mesoscale moisture transport and its effects on the daytime CI episode, variations in model initial conditions (including different initialization times and various initial perturbations) were performed and described in the following section.

First, two sensitivity experiments (INI12 and INI36) were initialized at different initialization times, including 00 UTC 5 September and 00 UTC 4 September, 12 and 36 hr prior to the CNTL, respectively. Both the INI12 and

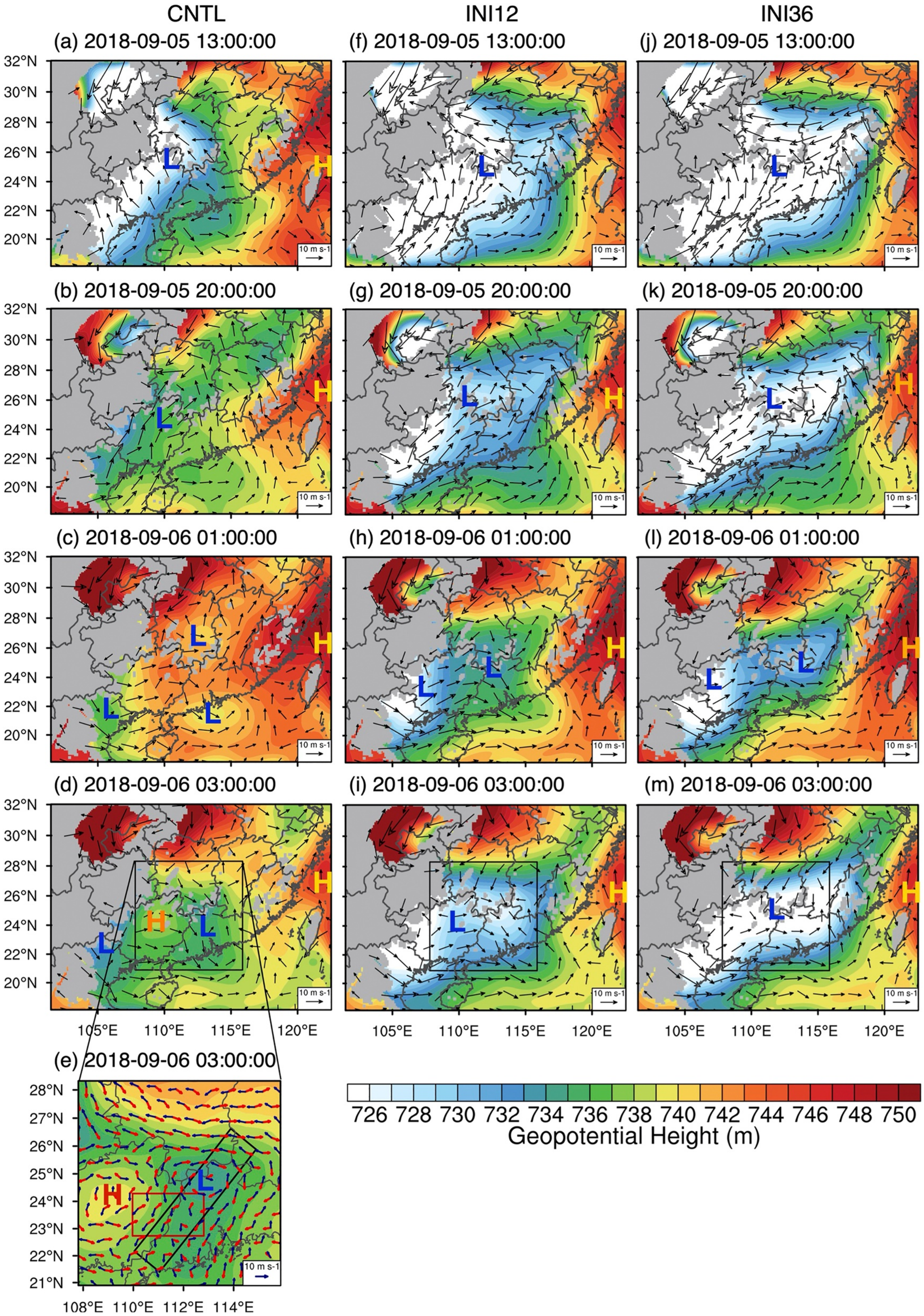

Figure 12. Evolution of simulated geopotential height (shaded) and horizontal wind fields (vector) at 925 hPa at (a, f, and j) 13 UTC 5 September (b, g and k) 20 UTC 5 September (c, h, and l) 01 UTC 6 September, and (d, i, and m) 03 UTC 6 September in (a–d) CNTL (f–i) INI12 and (j–m) INI36 runs. (e) Spatially filtered geopotential height (shaded), geostrophic winds (blue vector) and ageostrophic winds (red vector) at 925 hPa at 03 UTC 6 September in CNTL. High- and low-pressure systems are denoted by "H" and "L", respectively.

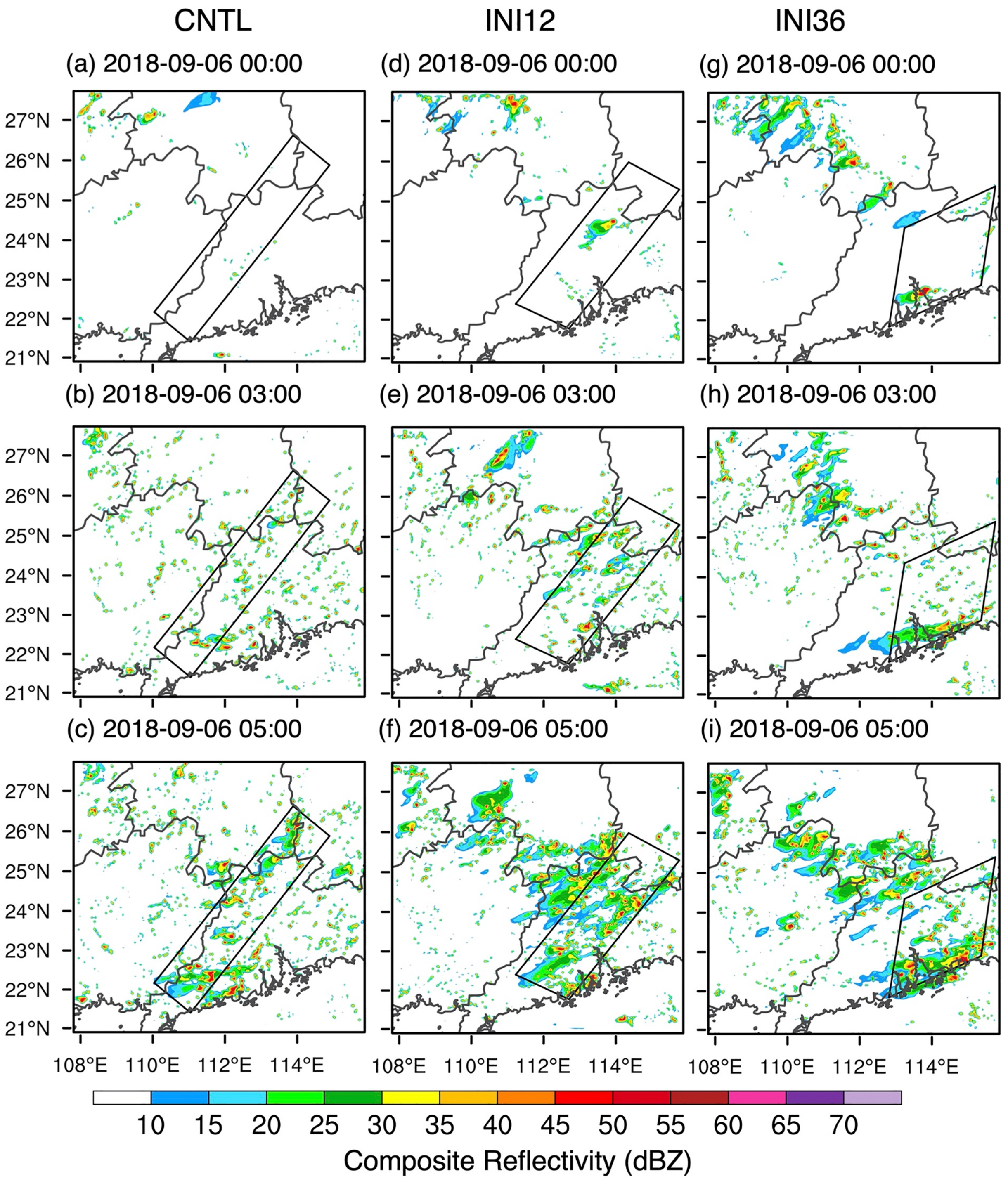

Figure 13. Horizontal distribution of simulated composite reflectivity at (a, d, and g) 00 UTC (b, e, and h) 03 UTC and (c, f, and i) 05 UTC 6 September 2018 in the (a–c) CNTL (d–f) INI12, and (g–i) INI36 runs. Black boxes represent the CI episode regions in each experiment.

INI36 runs showed the occurrence of CI episodes in a linear region at a similar time as the CNTL (approximately 03 UTC 6 September), but their locations and shapes were different (Figure 13). In the INI12 run, the CI episode region with a SW-NE orientation was located in the middle of Guangdong Province, which was farther east (~75 km) from that in the CNTL (cf. Figures 13b–13c and 13e–13f). In the INI36 run, the CI episode occurred

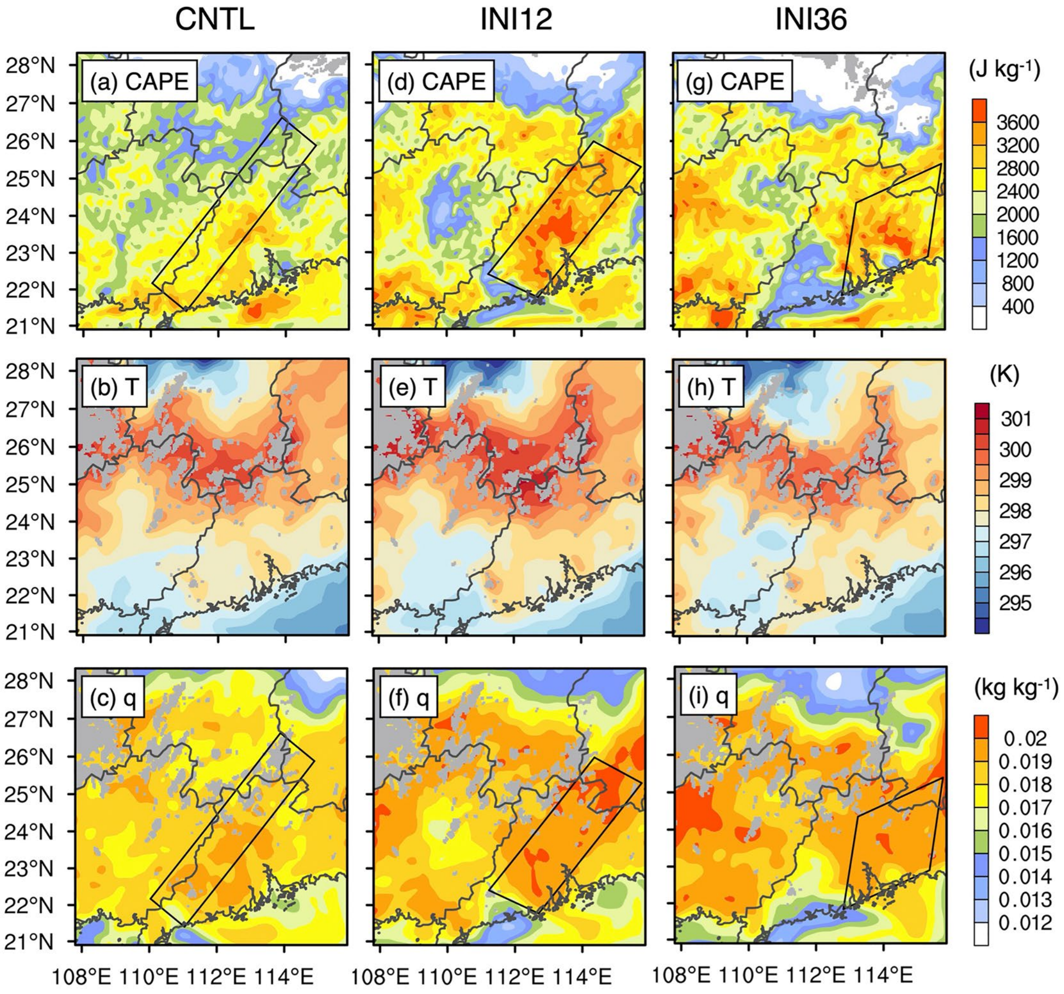

Figure 14. Simulated (a, d, and g) surface CAPE (b, e, and h) temperature at 925 hPa and (c, f, and i) specific humidity at 925 hPa at 03 UTC 6 September 2018 in the (a–c) CNTL (d–f) INI12, and (g–i) INI36 runs. Black boxes represent the CI episode regions in each experiment.

even farther east with more zonal orientation compared with the CNTL run (~200 km, ~14°, located in eastern Guangdong Province, cf. Figures 13b, 13c and 13h, 13i).

The two sensitivity experiments were both characterized by weak convergence for lifting as that in the CNTL (not shown). Figure 14 compares the horizontal distributions of thermodynamic conditions in the sensitivity and CNTL runs. The locations of the high CAPE regions differed from each other, which matched well with the corresponding CI episode region (black boxes in Figure 14). Horizontal distributions of low-level temperature were similar among these experiments (Figures 14b, 14e and 14h), and temperature inhomogeneity was not found between the CI episode regions and less-CI regions in those runs. In contrast, the regions with higher specific humidity varied in locations among the three experiments (Figures 14c, 14f and 14i). Since CAPE is affected by both temperature and humidity, the coincident distribution of CAPE and humidity verifies that the heterogeneity of CAPE was mainly contributed by the spatial variations in moisture in the present case. A similar sensitivity to moisture on CI timing can be seen in a case in eastern China documented by Luo and Chen (2015), where a larger amount of low-level moisture carried by monsoon airflow corresponded to an earlier timing of CI, while a more crucial role of temperature in controlling CI timing was found in a case that occurred in South China by Bao et al. (2020).

The sources for the different moisture distributions were further examined. In the INI12 and INI36 runs (Figures 8c–8f), each CI episode region obtained a net moisture flux input after 00 UTC similar to that of the CNTL run. In the three experiments, mesoscale anticyclonic moisture transport acted as the main contributor that transported net moisture fluxes entering through their SW-NE oriented boundaries (boundaries A and C). In the INI36 run, nearly no CI occurred over the original CI episode region in the CNTL run (indicated as "no-CI", red box in Figure 8e) because the net moisture input was correspondingly weak there (Figure 8f). More net moisture input occurred in eastern Guangdong than in western Guangdong (no-CI region) and thus favored CIs east of the episode region in the CNTL run.

All three experiments showed strong anticyclonic moisture transport as the source of additional instability, which caused northwesterly transport through boundary A near the western part of each CI episode region (Figure 9), but anticyclonic transport varied in locations. The anticyclonic transports located farther east in the INI12 and INI36 runs could deliver moisture farther east than in the CNTL run. The evolution of geopotential height at 925 hPa (Figure 12) was also illustrated to be linked to the various locations of horizontal moisture transport. A low-pressure vortex occurred in South China in the three experiments but was stronger in the INI12 run and strongest in the INI36 run (Figures 12a, 12f and 12j, indicated by "L"). Similarly, the low-pressure vortex weakened with the westward invasion of the neighboring subtropical high before 01 UTC 6 September (Figures 12b, 12g and 12k). Due to the stronger low-pressure vortex in the INI12 and INI36 runs, the subtropical high invaded westward more lightly (Figures 12g and 12k). Then, the low-pressure vortex was separated into two isolated low-pressure disturbances. The eastern one in INI12 was located farther east than the one in the CNTL run. In the INI36 run, the isolated mesoscale disturbance was much stronger and located farther east than that in the INI12 run. After 01 UTC 6 September, the subtropical high in the INI12 and INI36 runs did not invade the strong low-pressure vortex and did not isolate a mesoscale high-pressure disturbance on land as it did in the CNTL runs. Moisture from the Beibu Gulf was still transported with anticyclonic circulation but through airflow northwest of the subtropical high over the sea in the INI12 and INI36 runs (Figures 12i and 12m). The anticyclonic circulation was located farther east in the INI12 run and conveyed moisture to the middle of Guangdong (Figures 9f and 12i), while the anticyclonic circulation in the INI36 run transported moisture even farther east to eastern Guangdong (Figures 9i and 12m). The ageostrophic winds also played an essential role in the formation of anticyclonic transport in the INI12 and INI36 runs, as in the CNTL run (not shown).

These three sensitivity experiments showed diverse locations of mesoscale anticyclonic transport at different initialization times due to their distinct formations. The inhomogeneous distribution of instability by anticyclonic transport thus changed and finally moved into the locations of the subsequent CI episode region.

In addition, 20-member ensemble simulations were conducted by the WRF model with the same configuration as the CNTL run other than initial conditions from global ensemble forecast system (GEFS) data. Despite initial perturbations, the CI episode was generally well represented at the nearby location and had a similar linear shape in most ensemble members (Figure 15). Distinct from the large errors in different initialization times, the mesoscale low-pressure disturbances over South China and the mesoscale high-pressure disturbance were reproduced in small initial perturbation simulations well (not shown). The formation of mesoscale anticyclonic transport near the western border of the CI episode region was thus in good representation when considering the uncertainties in the input data, which contributed to good reproduction of CI episodes. In particular, the simulated CI episode region was located slightly farther east (~50 km) in member 03 and obviously farther east (~110 km) in member 11 (Figures 15c and 15k) than in CNTL. Correspondingly, the anticyclonic transport and the resulting more unstable regions in members 03 and 11 were located farther east than those in the CNTL run (Figures 16a, 16b and 16e, 16f). In member 08, stronger convection was simulated in the nearby CI episode region compared with the CNTL run (Figure 15h). Before initiation, stronger mesoscale anticyclonic transport formed more highly unstable conditions in the CI episode region (Figures 16c and 16g). Variations in mesoscale pressure disturbances generated from uncertainties in all sensitivity experiments resulted in the corresponding offsets of locations of mesoscale anticyclonic transport and the CI episode region. The above results further confirm the decisive role of mesoscale anticyclonic moisture transport on the location of daytime CI episodes revealed in the previous section.

8. Climatology of Daytime CI Episodes

Wilson and Roberts (2006) documented that CI episode events during IHOP showed a maximum during the daytime. Statistics on daytime CI episodes in South China were also conducted in this study. Quantitatively, the CI episode is defined as two or more convections initiated in a time interval less than 12 min, and the distance between each initiation should not exceed 50 km. We focused on the CI episode occurring during the daytime from 06 to 18 LT and irrelevant to preexisting storms.

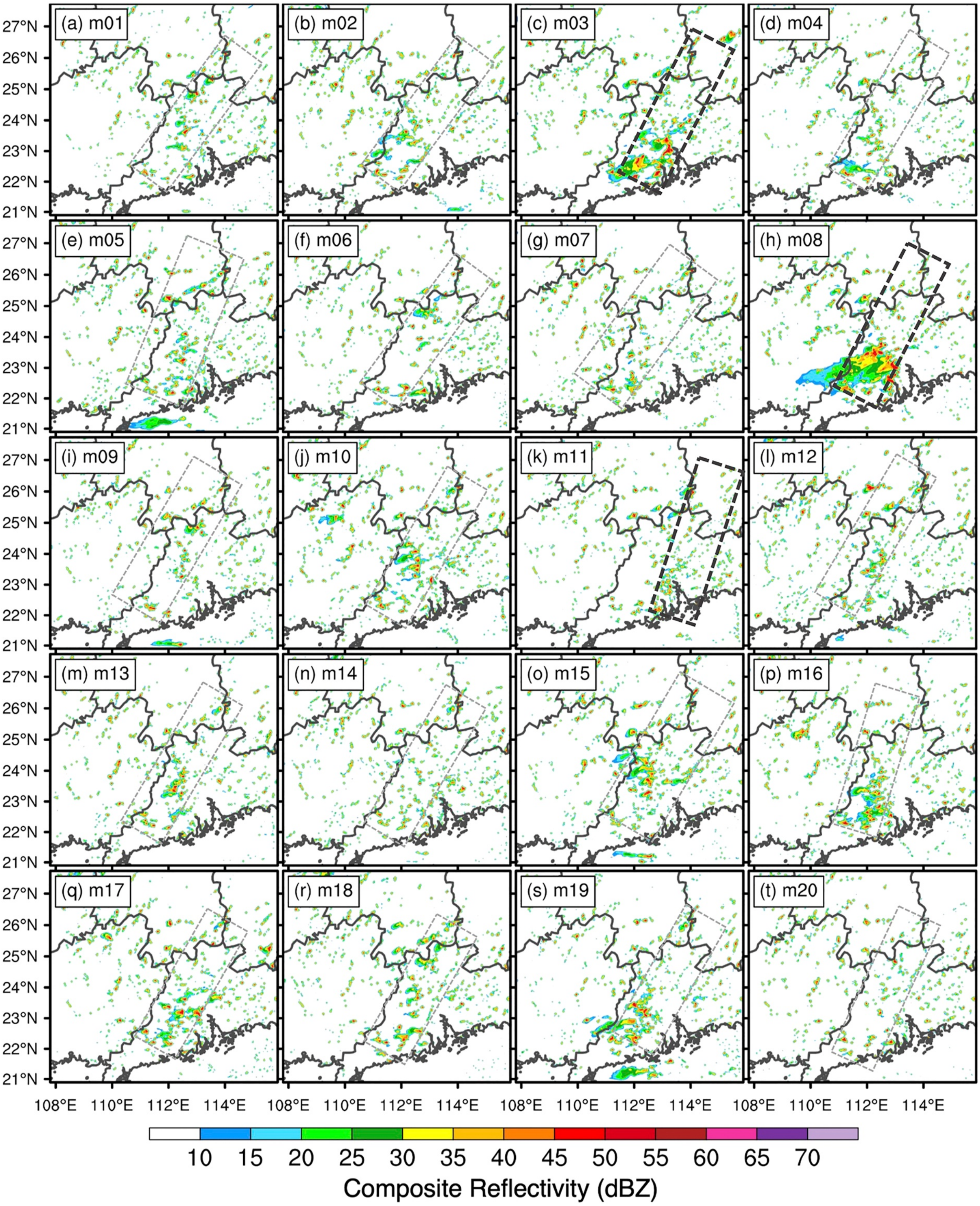

Figure 15. Simulated composite reflectivity of the 20 ensemble members at 03 UTC 6 September 2018. Black boxes represent the CI episode regions in every member.

In total, 92 daytime CI episodes were identified in 2018 over South China by 6-min mosaic radar products. The occurrence distribution of these daytime CI episodes is shown in Figure 17. CI episodes were active during 11–13 LT along the coastline or near mountains. However, these clustered CIs during the daytime also appeared in other areas. To determine where daytime CIs would statistically be clustered in, the environmental conditions

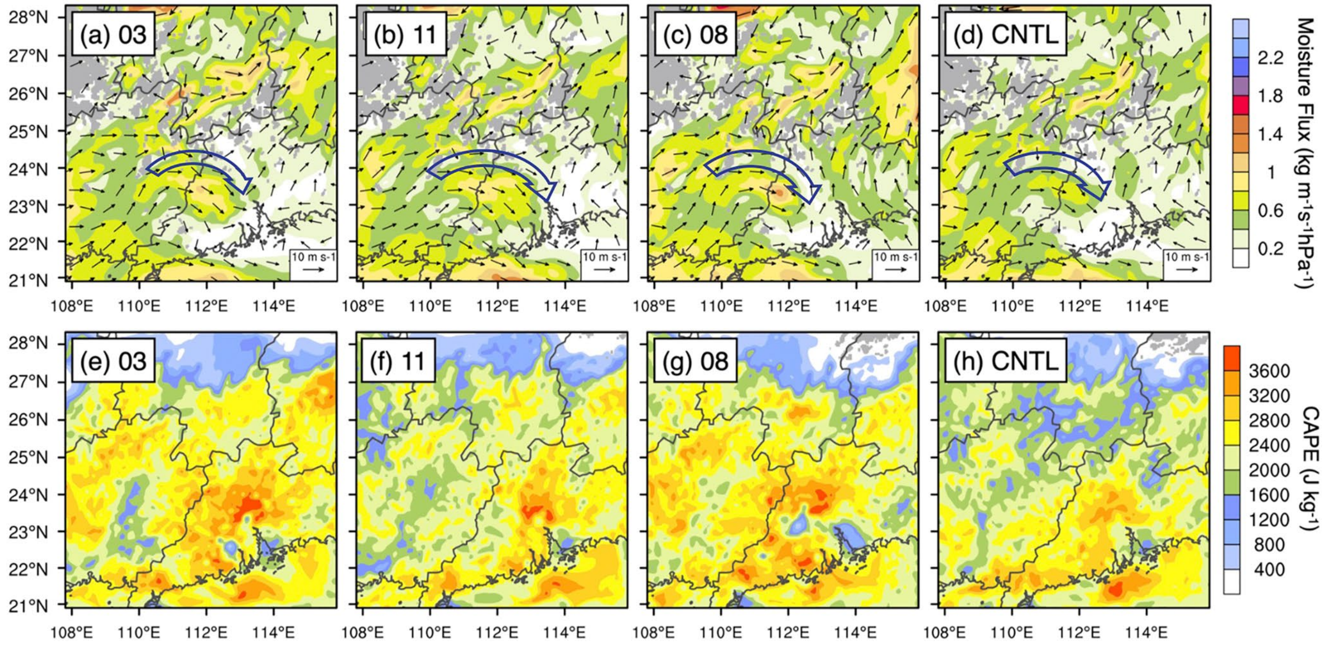

Figure 16. (a–d) Distributions of simulated moisture fluxes (shaded) and horizontal wind fields (vector) of ensemble members 03, 11, 08 and the CNTL run at 925 hPa at 00 UTC 6 September (e–h) CAPE of the three ensemble members and the CNTL run at 03 UTC 6 September. The thick blue vectors denote the mesoscale anticyclonic airflow.

from hourly ERA5 data around the central CI in each daytime CI episode were examined. Most daytime CI episodes occurred in a low-level weak convergent or even divergent precondition (Figure 18a), as in the case studied in the previous section, unlike the nocturnal CI episodes, which are usually located along strong convergence boundaries with widely varying possible mechanisms (e.g., M. R. Zhang et al., 2019; Reif & Bluestein, 2018; Wilson et al., 2018). The heterogeneity of composite moisture was also observed between the episode region and the surroundings (Figure 18b), similar to the current case. Figure 18c spatially averaged the specific humidity within 1° from the central location of the CI episode. On average, moisture around the center of the CI episode accumulated 7 hr before CI and reached a maximum as convection began to be triggered, creating a thermodynamically favorable environment for the daytime CI episode.

Next, the moisture transport for the heterogeneity of moisture near daytime CI episode regions was investigated. The moisture transport in each daytime CI episode was classified based on the prevailing low-level wind directions near the episode region from the south ocean, including southwesterly, southeasterly, southerly, anticyclonic, and

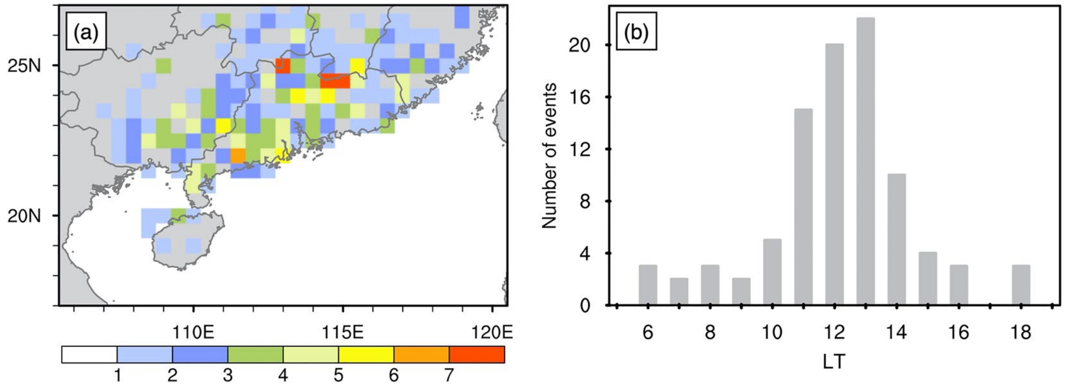

Figure 17. (a) CI occurrence distribution for daytime CI episodes and (b) diurnal variation of daytime CI episode occurrence during 2018.

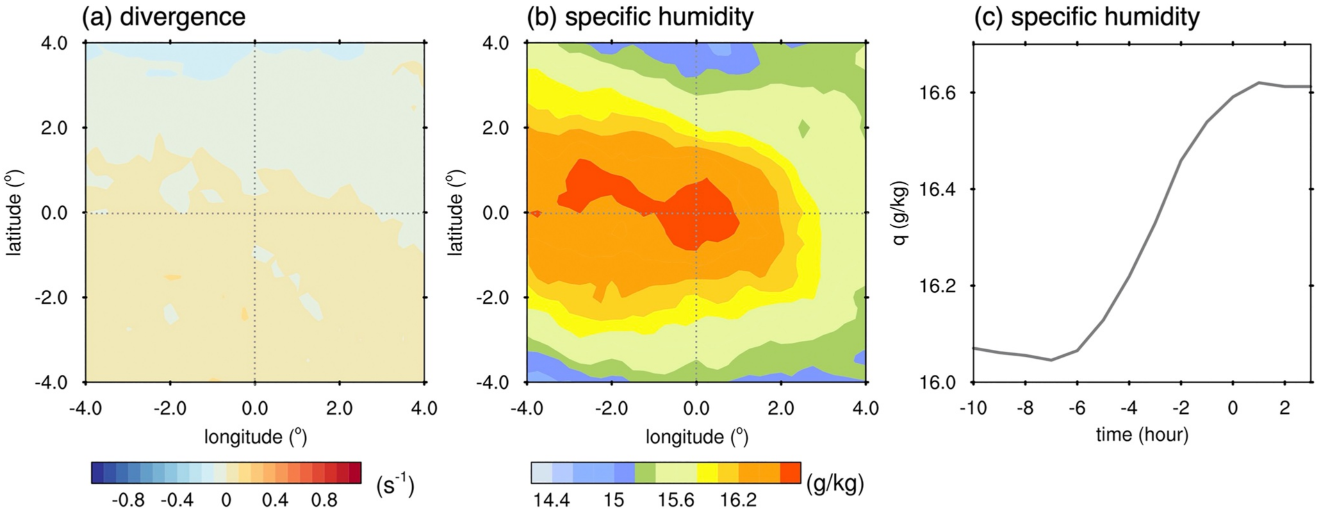

Figure 18. Composite of (a) divergence (s^{-1}), (b) specific humidity (g kg^{-1}) at 925 hPa around the central CI in each daytime CI episode at the initiation hour. (c) Composite time series of specific humidity (g kg^{-1}) at 925 hPa before and after the occurrence of the daytime CI episode.

cyclonic transports. CI episodes in the environment of low-level convergence were not included in the classification. Figure 19 presents a composite of moisture flux and winds at 925 hPa in each classification. In all types, the sources of enhanced moisture within the CI episode regions were the mesoscale transports that were strong at the central location of the CI episode, rather than large-scale moisture transport (Figure 19). Similar to the anticyclonic transport in the studied case, mesoscale transports carried moisture to the locations of the daytime CI episode region and thus enhanced the moisture in the episode regions and created additionally unstable conditions for triggering there.

9. Summary and Discussion

A large number of convective cells initiated and clustered in a region at a similar time are named CI episodes and are commonly formed under similar environmental conditions. Many previous studies have mainly focused on nocturnal CI episodes under unfavorable thermodynamic conditions and usually along various kinds of strong convergence boundaries (e.g., M. R. Zhang et al., 2019; Reif & Bluestein, 2018; Wilson et al., 2018). Clustered CIs are also commonly observed during the daytime, when a favorable unstable environment due to solar radiation is widely provided, but it is seldom revealed why additional instability and daytime CIs are confined within a certain region. Both observations and convection-permitting WRF simulations were performed to investigate the source of the inhomogeneous instability during a typical event of a daytime CI episode in South China. In the preconvective environment, extra CAPE accumulated in the CI episode region compared with the neighboring regions and had an additional transport of moisture.

The additionally enhanced moisture in the daytime CI episode region in the current case was a primary result of mesoscale anticyclonic moisture transport through the western boundary from the Beibu Gulf. The existence of anticyclonic moisture transport and its moistening were validated with observational evidence. Anticyclonic moisture transport formed under the effects of both nocturnal clockwise-rotating ageostrophic winds by inertial oscillation and mesoscale high-pressure disturbance-influenced geostrophic winds in the morning.

Sensitivity experiments initialized at different initial conditions were further conducted to verify the sources of the CI episode and to examine the sensitivity of mesoscale anticyclonic transport to model uncertainties. Stronger mesoscale pressure disturbances in initial conditions resulted in mesoscale anticyclonic airflows under various formation processes and conveyed moisture farther east; thus, the CI episode occurred farther east by dozens to hundreds of kilometers. The timing of the CI episode was in good agreement with the initial conditions in this case. The location errors of the CI episode in the present study largely depended on mesoscale moisture transport, which was sensitive to the bias of mesoscale disturbances.

Moisture transport through larger-scale airflows, such as monsoon flows or low-level jets, is commonly found and strengthens precipitation or thermodynamically supports nocturnal CIs in South China (e.g., Bai et al., 2020a; Du

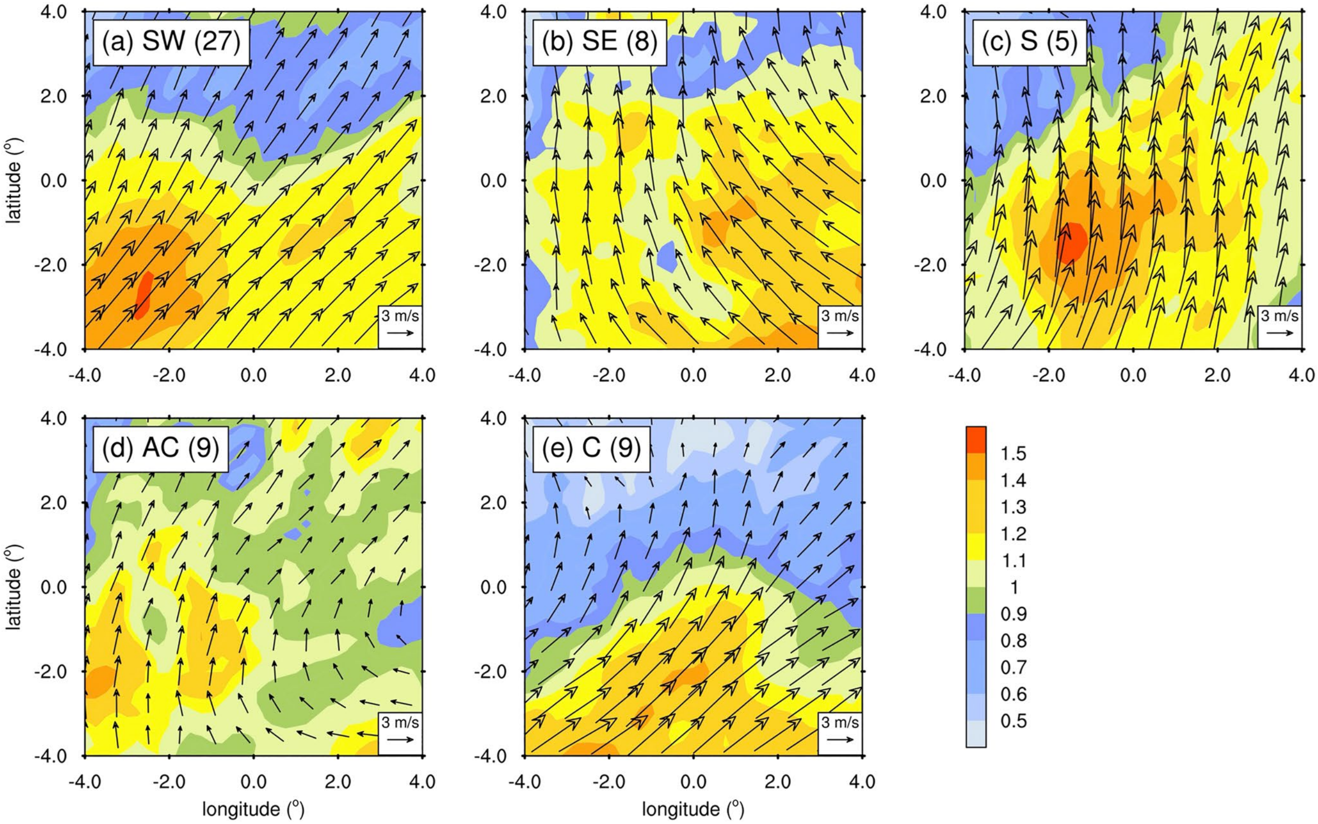

Figure 19. Composite of moisture flux (km m^{-1}s^{-1} hPa^{-1}, shaded) and wind field (m s^{-1}, vector) at 925 hPa around the central CI in each daytime CI episode for five mesoscale moisture transport types, including (a) southwesterly, (b) southeasterly, (c) southerly, (d) anticyclonic, and (e) cyclonic types. The numbers in brackets denote the number of cases in the classification.

& Chen, 2019a; Du, Chen, Han, Mai, et al., 2020). The mesoscale anticyclonic moisture transport that determines the location of the daytime CI episode in the current study is a new finding. The mesoscale anticyclonic moisture transport influenced by the mesoscale pressure disturbances was sensitive in the models and largely changed the locations of confined daytime CIs, thus a key for forecasting.

Statistics on daytime CI episodes in 2018 show a high frequency in South China and a wide possibility in locations. Unlike the widely revealed nocturnal CI episodes that prefer to occur along strongly convergent regions, this study found that the daytime CI episodes were in weak low-level convergence and clustered in moister patches. As in the studied case, mesoscale transports carried moisture to the episode regions to enhance low-level moisture and trigger a series of daytime CIs there. In addition to the mesoscale anticyclonic transport in the studied case, other types of mesoscale transport were also found, which might also be sensitive in models and largely influence the locations of daytime CI episodes, but more numerical studies are needed in the future.

Further studies also need to be conducted on the relationship between the predictability of mesoscale disturbances and the predictability of CIs. In addition to synoptic forcing (e.g., Hanley et al., 2011; Melhauser & Zhang, 2012), storm-scale or mesoscale environmental variations have been found to bring differences in the location and timing of CIs and even to the structure and ensuing development (Adler et al., 2011; Fabry, 2006). More daytime CI episode cases and related statistical studies will be examined in the future to find other sources of daytime CI episodes and to achieve a general understanding of daytime CI episodes.

Data Availability Statement

The surface, mosaic radar products and the sounding data used for observational verification are available at National Meteorological Information Center of the China Meteorological Administration via http://data.cma.

cn/data/. The NCEP FNL data used to show synoptic condition is available at NCAR via https://rda.ucar.edu/datasets/ds083.3/ (NCEP, 2015). Global ensemble forecast system data used as initial condition for ensemble simulation is available at NOAA via https://www.ncei.noaa.gov/products/weather-climate-models/global-ensemble-forecast (NOAA, 1993). The ERA5 reanalysis data is from ECMWF via https://cds.climate.copernicus.eu/cdsapp#!/dataset/reanalysis-era5-pressure-levels?tab=overview (Hersbach et al., 2018). Version 4.0 of the WRF model used for numerical simulation in this study can be accessed at https://www2.mmm.ucar.edu/wrf/users/download/get_source.html (Skamarock et al., 2019).

Acknowledgments

This study was supported by the Guangdong Major Project of Basic and Applied Basic Research (2020B0301030004), the National Natural Science Foundation of China (Grant Nos. 42122033, 41875055, and 42075006), and the Guangzhou Science and Technology Plan Projects (202002030346 and 202002030196).

References

Abulikemu, A., Wang, Y., Gao, R. X., Wang, Y., & Xu, X. (2019). A numerical study of convection initiation associated with a gust front in Bohai Bay region, North China. *Journal of Geophysical Research: Atmospheres*, *124*(24), 13843–13860. https://doi.org/10.1029/2019jd030883

Adler, B., Kalthoff, N., & Gantner, L. (2011). Initiation of deep convection caused by land-surface inhomogeneities in West Africa: A modelled case study. *Meteorology and Atmospheric Physics*, *112*(1–2), 15–27. https://doi.org/10.1007/s00703-011-0131-2

Bai, L., Meng, Z., Huang, Y., Zhang, Y., Niu, S., & Su, T. (2019). Convection initiation resulting from the interaction between a quasi-stationary dryline and intersecting gust fronts: A case study. *Journal of Geophysical Research: Atmospheres*, *124*(5), 2379–2396. https://doi.org/10.1029/2018jd029832

Bai, L. Q., Chen, G. X., & Huang, L. (2020). Convection initiation in monsoon coastal areas (South China). *Geophysical Research Letters*, *47*(11), e2020GL087035. https://doi.org/10.1029/2020GL087035

Bai, L. Q., Chen, G. X., & Huang, L. (2020). Image processing of radar mosaics for the climatology of convection initiation in South China. *Journal of Applied Meteorology and Climatology*, *59*(1), 65–81. https://doi.org/10.1175/Jamc-D-19-0081.1

Balaji, V., & Clark, T. L. (1988). Scale selection in locally forced convective fields and the initiation of deep cumulus. *Journal of the Atmospheric Sciences*, *45*(21), 3188–3211. https://doi.org/10.1175/1520-0469(1988)045<3188:SSILFC>2.0.CO;2

Bao, X., Luo, Y., & Gao, X. (2020). The synoptic impacts on the convection initiation of a warm-sector heavy rainfall event over coastal South China prior to the monsoon onset: A numerical modeling study. *Journal of Geophysical Research: Atmospheres*, *126*(14), e2020JD034335. https://doi.org/10.1029/2020jd034335

Barnes, S. L. (1964). A technique for maximizing details in numerical weather map analysis. *Journal of Applied Meteorology*, *3*(4), 396–409. https://doi.org/10.1175/1520-0450(1964)003<0396:ATFMDI>2.0.CO;2

Birch, C. E., Roberts, M. J., Garcia-Carreras, L., Ackerley, D., Reeder, M. J., Lock, A. P., & Schiemann, R. (2015). Sea-breeze dynamics and convection initiation: The influence of convective parameterization in weather and climate model biases. *Journal of Climate*, *28*(20), 8093–8108. https://doi.org/10.1175/JCLI-D-14-00850.1

Blackadar, A. K. (1957). Boundary layer wind maxima and their significance for the growth of nocturnal inversions. *Bulletin of the American Meteorological Society*, *38*(5), 283–290. https://doi.org/10.1175/1520-0477-38.5.283

Bodine, D., Heinselman, P. L., Cheong, B. L., Palmer, R. D., & Michaud, D. (2010). A case study on the impact of moisture variability on convection initiation using radar refractivity retrievals. *Journal of Applied Meteorology and Climatology*, *49*(8), 1766–1778. https://doi.org/10.1175/2010JAMC2360.1

Bolton, D. (1980). The computation of equivalent potential temperature. *Monthly Weather Review*, *108*(7), 1046–1053. https://doi.org/10.1175/1520-0493(1980)108<1046:TCOEPT>2.0.CO;2

Burghardt, B. J., Evans, C., & Roebber, P. J. (2014). Assessing the predictability of convection initiation in the high Plains using an object-based approach. *Weather and Forecasting*, *29*(2), 403–418. https://doi.org/10.1175/WAF-D-13-00089.1

Coniglio, M. C., Correia, J., Jr., Marsh, P. T., & Kong, F. (2013). Verification of convection-allowing WRF model forecasts of the planetary boundary layer using sounding observations. *Weather and Forecasting*, *28*(3), 842–862. https://doi.org/10.1175/WAF-D-12-00103.1

Crook, N. A. (1996). Sensitivity of moist convection forced by boundary layer processes to low-level thermodynamic fields. *Monthly Weather Review*, *124*(8), 1767–1785. https://doi.org/10.1175/1520-0493(1996)124<1767:SOMCFB>2.0.CO;2

Degelia, S. K., Wang, X., Stensrud, D. J., & Johnson, A. (2018). Understanding the impact of radar and in situ observations on the prediction of a nocturnal convection initiation event on 25 June 2013 using an ensemble-based multiscale data assimilation system. *Monthly Weather Review*, *146*(6), 1837–1859. https://doi.org/10.1175/MWR-D-17-0128.1

Du, Y., Chen, G., Han, B., Bai, L., & Li, M. (2020). Convection initiation and growth at the coast of South China. Part II: Effects of the terrain, coastline, and cold pools. *Monthly Weather Review*, *148*(9), 3871–3892. https://doi.org/10.1175/MWR-D-20-0090.1

Du, Y., Chen, G., Han, B., Mai, C., Bai, L., & Li, M. (2020). Convection initiation and growth at the coast of South China. Part I: Effect of the marine boundary layer jet. *Monthly Weather Review*, *148*(9), 3847–3869. https://doi.org/10.1175/mwr-d-20-0089.1

Du, Y., & Chen, G. X. (2019). Climatology of low-level jets and their impact on rainfall over southern China during early-summer rainy season. *Journal of Climate*, *32*(24), 8813–8833. https://doi.org/10.1175/JCLI-D-19-0306.1

Du, Y., & Chen, G. X. (2019). Heavy rainfall associated with double low-level jets over southern China. Part II: Convection initiation. *Monthly Weather Review*, *147*(2), 543–565. https://doi.org/10.1175/Mwr-D-18-0102.1

Ek, M. B., Mitchell, K. E., Lin, Y., Rogers, E., Grunmann, P., Koren, V., et al. (2003). Implementation of Noah land surface model advances in the National Centers for Environmental Prediction operational mesoscale Eta model. *Journal of Geophysical Research*, *108*(D22), 2002JD003296. https://doi.org/10.1029/2002jd003296

Fabry, F. (2004). Meteorological value of ground target measurements by radar. *Journal of Atmospheric and Oceanic Technology*, *21*(4), 560–573. https://doi.org/10.1175/1520-0426(2004)021<0560:MVOGTM>2.0.CO;2

Fabry, F. (2006). The spatial variability of moisture in the boundary layer and its effect on convection initiation: Project-long characterization. *Monthly Weather Review*, *134*(1), 79–91. https://doi.org/10.1175/MWR3055.1

Gebauer, J. G., Shapiro, A., Fedorovich, E., & Klein, P. (2018). Convection initiation caused by heterogeneous low-level jets over the Great Plains. *Monthly Weather Review*, *146*(8), 2615–2637. https://doi.org/10.1175/MWR-D-18-0002.1

Hanley, K. E., Kirshbaum, D. J., Belcher, S. E., Roberts, N. M., & Leoncini, G. (2011). Ensemble predictability of an isolated mountain thunderstorm in a high-resolution model. *Quarterly Journal of the Royal Meteorological Society*, *137*(661), 2124–2137. https://doi.org/10.1002/qj.877

Henderson, D. S., Otkin, J. A., & Mecikalski, J. R. (2021). Evaluating convective initiation in high-resolution numerical weather prediction models using GOES-16 infrared brightness temperatures. *Monthly Weather Review*, *149*(4), 1153–1172. https://doi.org/10.1175/MWR-D-20-0272.1

Hersbach, H., Bell, B., Berrisford, P., Biavati, G., Horányi, A., Muñoz Sabater, J., et al. (2018). ERA5 hourly data on pressure levels from 1979 to present [dataset]. Copernicus climate change service (C3S) climate data store (CDS). https://doi.org/10.24381/cds.bd0915c6

Iacono, M. J., Delamere, J. S., Mlawer, E. J., Shephard, M. W., Clough, S. A., & Collins, W. D. (2008). Radiative forcing by long-lived greenhouse gases: Calculations with the AER radiative transfer models. *Journal of Geophysical Research*, *113*(D13), D13103. Artn D13103. https://doi.org/10.1029/2008jd009944

Janjić, Z. I. (1994). The step-mountain eta coordinate model: Further developments of the convection, viscous sublayer, and turbulence closure schemes. *Monthly Weather Review*, *122*(5), 927–945. https://doi.org/10.1175/1520-0493(1994)122<0927:TSMECM>2.0.CO;2

Kain, J. S. (2004). The Kain-Fritsch convective parameterization: An update. *Journal of Applied Meteorology*, *43*(1), 170–181. https://doi.org/10.1175/1520-0450(2004)043<0170:Tkcpau>2.0.Co;2

Lima, M. A., & Wilson, J. W. (2008). Convective storm initiation in a moist tropical environment. *Monthly Weather Review*, *136*(6), 1847–1864. https://doi.org/10.1175/2007MWR2279.1

Luo, Y., & Chen, Y. (2015). Investigation of the predictability and physical mechanisms of an extreme-rainfall-producing mesoscale convective system along the Meiyu front in East China: An ensemble approach. *Journal of Geophysical Research: Atmospheres*, *120*(20), 10–593. https://doi.org/10.1002/2015JD023584

Melhauser, C., & Zhang, F. (2012). Practical and intrinsic predictability of severe and convective weather at the mesoscales. *Journal of the Atmospheric Sciences*, *69*(11), 3350–3371. https://doi.org/10.1175/JAS-D-11-0315.1

Moore, J. T., Glass, F. H., Graves, C. E., Rochette, S. M., & Singer, M. J. (2003). The environment of warm-season elevated thunderstorms associated with heavy rainfall over the central United States. *Weather and Forecasting*, *18*(5), 861–878. https://doi.org/10.1175/1520-0434(2003)018<0861:TEOWET>2.0.CO;2

National Centers for Environmental Prediction/National Weather Service/NOAA/U.S. Department of Commerce. (2015). NCEP FNL operational model global tropospheric analyses, continuing from July 1999 [dataset]. Research Data Archive at the National Center for Atmospheric Research, Computational and Information Systems Laboratory. https://doi.org/10.5065/D65Q4T4Z

NOAA National Centers for Environmental Information. (1993). Global ensemble forecast system [dataset]. NOAA National Centers for Environmental Information. Retrieved from https://www.ncei.noaa.gov/products/weather-climate-models/global-ensemble-forecast

Otkin, J. A., & Greenwald, T. J. (2008). Comparison of WRF model-simulated and MODIS-derived cloud data. *Monthly Weather Review*, *136*(6), 1957–1970. https://doi.org/10.1175/2007MWR2293.1

Parsons, D. B., Haghi, K. R., Halbert, K. T., Elmer, B., & Wang, J. H. (2019). The potential role of atmospheric bores and gravity waves in the initiation and maintenance of nocturnal convection over the southern Great Plains. *Journal of the Atmospheric Sciences*, *76*(1), 43–68. https://doi.org/10.1175/Jas-D-17-0172.1

Radhakrishna, B., Fabry, F., Braun, J. J., & Van Hove, T. (2015). Precipitable water from GPS over the continental United States: Diurnal cycle, intercomparisons with NARR, and link with convective initiation. *Journal of Climate*, *28*(7), 2584–2599. https://doi.org/10.1175/JCLI-D-14-00366.1

Reif, D. W., & Bluestein, H. B. (2018). Initiation mechanisms of nocturnal convection without nearby surface boundaries over the central and southern Great Plains during the warm season. *Monthly Weather Review*, *146*(9), 3053–3078. https://doi.org/10.1175/MWR-D-18-0040.1

Skamarock, W. C., Klemp, J. B., Dudhia, J., Gill, D. O., Liu, Z., Berner, J., & Huang, X. Y. (2019). A description of the advanced research WRF model version 4 [software]. National Center for Atmospheric Research. https://doi.org/10.5065/1dfh-6p97

Thompson, G., Field, P. R., Rasmussen, R. M., & Hall, W. D. (2008). Explicit forecasts of winter precipitation using an improved bulk microphysics scheme. Part II: Implementation of a new snow parameterization. *Monthly Weather Review*, *136*(12), 5095–5115. https://doi.org/10.1175/2008mwr2387.1

Torri, G., Kuang, Z. M., & Tian, Y. (2015). Mechanisms for convection triggering by cold pools. *Geophysical Research Letters*, *42*(6), 1943–1950. https://doi.org/10.1002/2015gl063227

Trier, S. B., Kehler, S., & Hanesiak, J. (2020). Observations and simulation of elevated nocturnal convection initiation on 24 June 2015 during PECAN. *Monthly Weather Review*, *148*(2), 613–635. https://doi.org/10.1175/Mwr-D-19-0218.1

Trier, S. B., Wilson, J. W., Ahijevych, D. A., & Sobash, R. A. (2017). Mesoscale vertical motions near nocturnal convection initiation in PECAN. *Monthly Weather Review*, *145*(8), 2919–2941. https://doi.org/10.1175/Mwr-D-17-0005.1

Wang, H., Luo, Y., & Jou, B. J.-D. (2014). Initiation, maintenance, and properties of convection in an extreme rainfall event during SCMREX: Observational analysis. *Journal of Geophysical Research: Atmospheres*, *119*(23), 13–206. https://doi.org/10.1002/2014JD022339

Weckwerth, T. M. (2000). The effect of small-scale moisture variability on thunderstorm initiation. *Monthly Weather Review*. https://doi.org/10.1175/1520-0493(2000)129<4017:TEOSSM>2.0.CO;2

Weckwerth, T. M., Bennett, L. J., Jay Miller, L., Van Baelen, J., Di Girolamo, P., Blyth, A. M., & Hertneky, T. J. (2014). An observational and modeling study of the processes leading to deep, moist convection in complex terrain. *Monthly Weather Review*, *142*(8), 2687–2708. https://doi.org/10.1175/MWR-D-13-00216.1

Weckwerth, T. M., Hanesiak, J., Wilson, J. W., Trier, S. B., Degelia, S. K., Gallus, W. A., Jr., et al. (2019). Nocturnal convection initiation during PECAN 2015. *Bulletin of the American Meteorological Society*, *100*(11), 2223–2239. https://doi.org/10.1175/BAMS-D-18-0299.1

Weckwerth, T. M., & Parsons, D. B. (2006). A review of convection initiation and motivation for IHOP_2002. *Monthly Weather Review*, *134*(1), 5–22. https://doi.org/10.1175/Mwr3067.1

Weckwerth, T. M., Wilson, J. W., & Wakimoto, R. M. (1996). Thermodynamic variability within the convective boundary layer due to horizontal convective rolls. *Monthly Weather Review*, *124*(5), 769–784. https://doi.org/10.1175/1520-0493(1996)1242.0.CO;2

Wilson, J. W., & Roberts, R. D. (2006). Summary of convective storm initiation and evolution during IHOP: Observational and modeling perspective. *Monthly Weather Review*, *134*(1), 23–47. https://doi.org/10.1175/Mwr3069.1

Wilson, J. W., Trier, S. B., Reif, D. W., Roberts, R. D., & Weckwerth, T. M. (2018). Nocturnal elevated convection initiation of the PECAN 4 July hailstorm. *Monthly Weather Review*, *146*(1), 243–262. https://doi.org/10.1175/Mwr-D-17-0176.1

Wu, M., & Luo, Y. (2016). Mesoscale observational analysis of lifting mechanism of a warm-sector convective system producing the maximal daily precipitation in China mainland during pre-summer rainy season of 2015. *Journal of Meteorological Research*, *30*(5), 719–736. https://doi.org/10.1007/s13351-016-6089-8

Xue, M., Luo, X., Zhu, K. F., Sun, Z. Q., & Fei, J. F. (2018). The controlling role of boundary layer inertial oscillations in Meiyu frontal precipitation and its diurnal cycles over China. *Journal of Geophysical Research: Atmospheres*, *123*(10), 5090–5115. https://doi.org/10.1029/2018jd028368

Zhang, F., Zhang, Q., & Sun, J. (2021). Initiation of an elevated mesoscale convective system with the influence of complex terrain during Meiyu season. *Journal of Geophysical Research: Atmospheres*, *126*(1), e2020JD033416. https://doi.org/10.1029/2020jd033416

Zhang, M. R., Meng, Z. Y., Huang, Y. P., & Wang, D. Y. (2019). The mechanism and predictability of an elevated convection initiation event in a weak-lifting environment in central-eastern China. *Monthly Weather Review*, *147*(5), 1823–1841. https://doi.org/10.1175/Mwr-D-18-0400.1

Zhang, S. S., Parsons, D. B., & Wang, Y. (2020). Wave disturbances and their role in the maintenance, structure, and evolution of a mesoscale convection system. *Journal of the Atmospheric Sciences*, *77*(1), 51–77. https://doi.org/10.1175/Jas-D-18-0348.1

Zhang, Y., Xue, M., Zhu, K., & Zhou, B. (2019). What is the main cause of diurnal variation and nocturnal peak of summer precipitation in Sichuan Basin, China? The key role of boundary layer low-level jet inertial oscillations. *Journal of Geophysical Research: Atmospheres*, *124*(5), 2643–2664. https://doi.org/10.1029/2018JD029834